A Unified Scheme to Solving Arbitrary Complex-valued Ratio Distribution with Application to Statistical Inference for Frequency Response Functions and Transmissibility Functions

Wang-Ji Yan*[1], Meng-Yun Zhao[2], Michael Beer[3], Wei-Xin Ren*[4], Dimitrios Chronopoulos[5]

[1]*State Key Laboratory of Internet of Things for Smart City and Department of Civil and Environmental Engineering, University of Macau, China*

[2]*Department of Civil Engineering, Hefei University of Technology, Anhui, China*

[3]*Institute for Risk and Reliability, Leibniz Universität Hannover, Germany*

[4]*Depart of Civil Engineering, Shenzhen University, Shenzhen, China*

[5]*Institute for Aerospace Technology & The Composites Group, The University of Nottingham, United Kingdom*

Abstract: Complex-valued ratio distributions arises in many real applications such as statistical inference for frequency response functions (FRFs) and transmissibility functions (TFs) in structural health monitoring. As a sequel to our previous study, a unified scheme to solving complex ratio random variables is proposed in this study for the case when it is highly non-trivial or impossible to discover a closed-form solution. Based on the probability transformation principle in the complex-valued domain, a unified formula is derived by reducing the concerned problem into multi-dimensional integrals, which can be solved by advanced numerical techniques. A fast Sparse-Grid Quadrature (SGQ) scheme by constructing multivariate quadrature formulas using the combinations of tensor products of suitable one-dimensional formulas is utilized to improve the computational efficiency by avoiding the problem of curse of integral dimensionality. The unified methodology enables the efficient and effective calculation of the PDF of a ratio random variable with its denominator and nominator specified by arbitrary probability distributions including Gaussian or non-Gaussian ratio random variables, correlated or independent random variables, bounded or unbounded ratio random variables. The unified scheme is applied to uncertainty quantification for FRFs and TFs, and the efficiency of the proposed scheme is verified by using the vibration test field data from a simply supported beam and from the Alamosa Canyon Bridge.

Keywords: Probability density function; Frequency response function; Transmissibility function; Complex ratio distribution; Sparse-Grid Quadrature rule; Structural health monitoring

*Corresponding author.
E-mail address: wangjiyan@um.edu.mo (W.J. Yan); renwx@szu.edu.cn (W.X. Ren)

1 Introduction

In engineering science, the ratio function defined as the quotient of two variables plays an important role in various fields. Uncertainty quantification for ratio random variables arises in many applied problems such as specifying the eigenvalue ratio distribution in cooperative spectrum sensing in cognitive radio [1], mass to energy ratios in nuclear physics, Mendelian inheritance ratios in genetics, and inventory ratios in economics, etc. Probability density functions (PDF) are usually regarded as one of the most versatile models to quantify the uncertainty comprehensively [2-4]. As popular statistical models, the Cauchy distribution, t-distribution and F-distribution are commonly-taught ratio distributions in statistical textbooks. Over the past few decades, the PDFs of ratio random variables including the Gaussian distribution family [5], t distribution family [6], chi-square family [7] and Bessel family [8], etc. have been studied extensively by a number of researchers.

It is worth noting that most of the efforts mentioned in the above are devoted to real-valued cases. Nowadays, the distributional properties of ratios of complex Gaussian random variables appear in many problems [9-14]. Baxley and his co-workers [10] derived the PDF for a ratio of correlated zero-mean complex Gaussian random variables based on the derivative of the Cumulative Density Function (CDF). The PDF for independent non-zero mean complex Gaussian ratios as a confluent hypergeometric function of the first kind was derived by Nadimi et al. in [15]. Nadarajah and Kwong [16] derived a closed-form PDF based on Nadimi's formula. New results for the statistics of the ratio of two complex Gaussian random variables where the numerator and denominator may have arbitrary means or variances and are possibly correlated were derived in [17]. A maximum-likelihood (ML) estimator was derived by Wu and Hughes [12] for antenna impedance in the form of a complex Gaussian ratio and proved its first absolute moment is finite yet mean-square unbounded. More recently, the moments of general complex Gaussian ratios whose numerator and denominator are correlated and have arbitrary mean were studied in [18], which proved that the mean-square and higher order absolute moments were unbounded in general. New theorems on multivariate circularly-symmetric complex Gaussian ratio distribution were proved on the basis of principle of probabilistic transformation of continuous random vectors in [19], which was then extended to the generalized non-zero mean proper multivariate complex Gaussian ratio distribution in [20].

In the field of dynamics, the dynamic characterization functions including frequency response functions (FRF) [20-23] and transmissibility functions (TF) [24-26] defined as the ratios of two frequency-domain responses also fall into the category of complex ratio random variables. As the most prevalent frequency domain tools, FRFs represent input-output relationships, while TFs are a mathematical representation of output-to-output relationships. Due to their clear physical interpretations, FRFs and TFs are of fundamental importance in damage detection [27-32], modal analysis [33-36], model updating [37,38], operational path analysis [39] and vibration isolation [40], etc.

It is worth mentioning here that both FRFs and TFs are estimated based on FFT coefficients, which inevitably involve different sources of uncertainties due to the inherent randomness of excitation [41], the variability of environmental conditions [42], as well as the numerical errors caused by discrete signals. Therefore, the results of complex ratio functions obtained via deterministic analysis methods without considering randomness related to FFT coefficients involved in engineering can deviate from the actual values significantly. As a result, quantifying the uncertainty for FRFs and TFs provides a fundamental way for improving the robustness of real applications.

Different approaches have been proposed to investigate the uncertainty of FRFs and TFs. Mao and Todd [23, 24] presented an analytical probabilistic model to quantify the uncertainty of FRFs and TFs using a Gaussian bivariate statistical model. However, the models are still restricted to a real-valued domain. Over the past few years, new theorems on circularly-symmetric complex Gaussian ratio distributions [19] as well as generalized complex Gaussian ratio distributions [20] have been proven mathematically to quantify the statistical distribution of FRFs and TFs. Unfortunately, these probabilistic models can only be utilized to characterize the uncertainty of FRFs and TFs when FFT coefficients follow complex Gaussian distributions. Recent research has revealed that the FFT coefficients may deviate from a Gaussian distribution and the complex t distribution was proposed to characterize some FFT coefficients with high kurtosis and heavy tails [43]. It is highly non-trivial or impossible to discover a closed-form solution for non-Gaussian complex-valued ratio distribution. Therefore, there is a need to propose a more versatile way to compute the ratio distribution with its numerator and denominator following arbitrary complex-valued probability distributions.

In this study, a unified scheme is presented to efficiently calculate the PDF of a complex-valued ratio random variable with its denominator and numerator specified by arbitrary complex-valued distributions. With the use of probability density transformation principle in the complex domain, a unified formula is derived for complex ratio distributions by reducing the concerned problem into multi-dimensional integrals. When it is difficult or impossible to discover a closed-form solution, one ought to resort to numerical algorithms. For Gaussian quadrature rule, the number of points to be calculated increases exponentially with the dimension of integrals, leading to uncomfortable computational burden. In this study, a novel SGQ formula based on the Smolyak rule [44] will be employed to address the curse of dimensionality problem. The sparse-grid method utilizes a linear combination of lower-level tensor products of univariate quadrature rules to approximate multivariate integrals [45,46]. Then the univariate quadrature point sets are extended to form a multi-dimensional grid using the sparse-grid theory [47,48]. The locations and weights of the univariate quadrature points corresponding to a range of accuracy levels can be determined by an asymptotic approximation method. Unlike the Gaussian quadrature formula, the accuracy of the SGQ rule can be flexibly controlled [49]. The method proposed in this paper can tackle various cases including the ratio of Gaussian and non-Gaussian random variables, correlated and independent random variables, as well as infinite and finite interval random variables.

The organization of this paper is as follows. Section 2 presents the theoretical background and the unified formula of complex ratio distributions expressed in terms of multi-dimensional integrals based on the principle of probability transformation in the complex domain. The SGQ formula based on the Smolyak rule is introduced in Section 3 to address the computational burden of multi-dimensional integrals involved in the unified formula of complex ratio distributions. The theoretical basics and developments from Section 2 and Section 3 are then utilized to infer the statistics of FRFs and TFs in Section 4. Two case studies are conducted in Section 5 to verify the unified formula of complex ratio distributions solved using SGQ strategy.

2 A Unified Scheme to Solving Complex Ratio Distribution

2.1 Some basic definitions

This study concerns the distribution of $\mathcal{Z} \in \mathbb{C}$ formulated as the ratio of two complex-valued random variables:

$$\mathcal{Z} = \frac{U}{V} = \frac{U^{\Re} + iU^{\Im}}{V^{\Re} + iV^{\Im}} \tag{1}$$

Where $i = \sqrt{-1}$; $U^{\Re}$ and $U^{\Im}$ denote the real and imaginary parts of U, while $V^{\Re}$ and $V^{\Im}$ denote the real and imaginary parts of V.

In the available references, the most common way of computing the distribution of ratio random variables is based on the definition of PDF by taking the derivative of the Cumulative Distribution Function (CDF) [10]. The complex-valued random variable $\mathcal{Z}$ is defined as $\mathcal{Z} = \mathcal{Z}^{\Re} + i\mathcal{Z}^{\Im}$, where $\mathcal{Z}^{\Re}$ and $\mathcal{Z}^{\Im}$ are a pair of real-valued random variables. $\mathcal{Z}$ is identified with the joint distribution of its real and imaginary parts $\left[\mathcal{Z}^{\Re}, \mathcal{Z}^{\Im}\right]$ as [50]:

$$\mathcal{F}_{\mathcal{Z}}(z)=\mathcal{F}_{\mathcal{Z}^{\Re},\mathcal{Z}^{\Im}}\left(z^{\Re},z^{\Im}\right)=p\left(\mathcal{Z}^{\Re}\le z^{\Re},\mathcal{Z}^{\Im}\le z^{\Im}\right) \tag{2}$$

where $\mathcal{F}_{\mathcal{Z}}(z)$ and $\mathcal{F}_{\mathcal{Z}^{\Re},\mathcal{Z}^{\Im}}\left(z^{\Re},z^{\Im}\right)$ are the CDF of complex random variable $\mathcal{Z}$ and joint distribution function of bivariate random vector $\left[\mathcal{Z}^{\Re},\mathcal{Z}^{\Im}\right]$, respectively. If $\mathcal{F}_{\mathcal{Z}^{\Re},\mathcal{Z}^{\Im}}\left(z^{\Re},z^{\Im}\right)$ is differentiable in $z^{\Re}$ and $z^{\Im}$, the following function is defined as PDF of the random variable z [10]:

$$p_{\mathcal{Z}}(z)=p_{\mathcal{Z}^{\Re},\mathcal{Z}^{\Im}}\left(z^{\Re},z^{\Im}\right)=\frac{\partial^2}{\partial z^{\Re}\partial z^{\Im}}\mathcal{F}_{z^{\Re},z^{\Im}}(z^{\Re},z^{\Im}) \tag{3}$$

From the above formulas, one can find that the solution involves complicated formula of CDF and partial derivatives. To avoid the difficulty of computing the CDFs and its partial derivatives, the principle of probabilistic transformation of random variables in the complex domain will be used in this study. As a result, complex ratio random variable following arbitrary distribution can reduce to a unified formula involving multi-dimensional integrals.

2.2 Linear probabilistic transformation in the complex domain

In the real-valued domain, if an n_o-variate random vector $\mathbf{X}=\left(X_1,X_2,\cdots,X_{n_o}\right)^T$ has a joint PDF $p_{\mathbf{X}}(\mathbf{x})$ with the value $\mathbf{x}=\left(x_1,x_2,\cdots,x_{n_o}\right)^T$, while a one-to-one and onto function is denoted by $\mathbf{s}=\mathcal{G}(\mathbf{x})=\left(\mathcal{G}_1(\mathbf{x}),\mathcal{G}_2(\mathbf{x}),\cdots,\mathcal{G}_{n_o}(\mathbf{x})\right)^T$; the inverse function of $\mathbf{s}=\mathcal{G}(\mathbf{x})$ is denoted by $\mathbf{x}=\mathcal{Q}(\mathbf{s})=\mathcal{G}^{-1}(\mathbf{s})$. The principle of probabilistic transformation of random vectors states that the PDF of a transformed random vector $\mathbf{s}=\mathcal{G}(\mathbf{x})$ is given by [51]:

$$p_{\mathbf{S}}(\mathbf{s})=\left|\mathcal{J}_{\mathcal{G}}\left(\mathcal{Q}(\mathbf{s})\right)\right|^{-1}p_{\mathbf{X}}\left(\mathcal{Q}(\mathbf{s})\right) \tag{4}$$

where $\mathcal{J}_{\mathcal{G}}\left(\mathcal{Q}(\mathbf{s})\right)$ denotes the Jacobian matrix given by:

$$\mathcal{J}_{\mathcal{G}}\left(\mathcal{Q}(\mathbf{s})\right)=\partial\left(\mathcal{G}_1,\mathcal{G}_2,\cdots,\mathcal{G}_{n_o}\right)\Big/\partial\left(x_1,x_2,\cdots,x_{n_o}\right) \tag{5}$$

Assume that two complex-valued random vectors $\mathbf{R}$ relates to $\boldsymbol{\Theta}$ through a linear transformation:

$$\mathbf{R}=\mathbf{W}\Theta \tag{6}$$

where $\mathbf{R}=\mathbf{R}^{\Re}+\mathbf{i}\mathbf{R}^{\Im}$, $\mathbf{W}=\mathbf{W}^{\Re}+\mathbf{i}\mathbf{W}^{\Im}$ and $\Theta=\Theta^{\Re}+\mathbf{i}\Theta^{\Im}$. The above equation can be rearranged as:

$$\begin{Bmatrix}\mathbf{R}^{\Re}\\ \mathbf{R}^{\Im}\end{Bmatrix}=\begin{bmatrix}\mathbf{W}^{\Re} & -\mathbf{W}^{\Im}\\ \mathbf{W}^{\Im} & \mathbf{W}^{\Re}\end{bmatrix}\begin{Bmatrix}\Theta^{\Re}\\ \Theta^{\Im}\end{Bmatrix} \tag{7}$$

A complex random vector is specified by the joint distribution of its real and imaginary parts, i.e. $p_{\mathbf{R}}(\mathbf{r})=p_{\mathbf{R}^{\Re},\mathbf{R}^{\Im}}(\mathbf{r}^{\Re},\mathbf{r}^{\Im})$ and $p_{\Theta}(\theta)=p_{\Theta^{\Re},\Theta^{\Im}}(\theta^{\Re},\theta^{\Im})$. According to the principle of probabilistic transformation of real random vectors, the joint PDF of $(\mathbf{R}^{\Re},\mathbf{R}^{\Im})$ is equal to [19,20]:

$$p_{\mathbf{R}}(\mathbf{r})=p_{\mathbf{R}^{\Re},\mathbf{R}^{\Im}}(\mathbf{r}^{\Re},\mathbf{r}^{\Im})=\left|\mathcal{J}_{\mathcal{W}}\right|^{-1}p_{\Theta}(\theta) \tag{8}$$

where $\mathcal{J}_{\mathcal{W}}=\begin{bmatrix}\mathbf{W}^{\Re} & -\mathbf{W}^{\Im}\\ \mathbf{W}^{\Im} & \mathbf{W}^{\Re}\end{bmatrix}$, and correspondingly, the determinant $\left|\mathcal{J}_{\mathcal{W}}\right|$ is given by:

$$\left|\mathcal{J}_{\mathcal{W}}\right|=\begin{vmatrix}\mathbf{w}^{\Re} & -\mathbf{w}^{\Im}\\ \mathbf{w}^{\Im} & \mathbf{w}^{\Re}\end{vmatrix}=\left|\mathbf{w}\mathbf{w}^{*}\right|=\left|\mathbf{w}\right|^{2} \tag{9}$$

Substituting Eq.(9) into Eq. (8) leads to the PDF of $\mathbf{R}$:

$$p_{\mathbf{R}}(\mathbf{r})=\left|\mathbf{w}\right|^{-2}p_{\Theta}(\theta) \tag{10}$$

2.3 The unified formula of complex ratio distribution

Since the complex ratio random variable $\mathcal{Z}=\dfrac{U}{V}$ is evolved from complex random variables $\{V,U\}^{T}\in\mathbb{C}^{2}$, it is intuitive to conceive the idea of deriving the PDF of $\mathcal{Z}$ using the principle of probabilistic transformation of a random vector in the complex domain introduced in the last section. However, the application of the principle of probabilistic transformation of random vectors should formulate a functional relationship between $\mathcal{Z}$ and $\{V, U\}^T$. To realize such a transformation, an auxiliary variable V is herein introduced to ensure that $\mathcal{Z}$ and $\{V, U\}^T$ have the same order:

$$\begin{Bmatrix} V \\ \mathcal{Z} \end{Bmatrix} = \begin{bmatrix} 1 & 0 \\ 0 & V^{-1} \end{bmatrix} \begin{Bmatrix} V \\ U \end{Bmatrix} \tag{11}$$

Using Eq.(6) with $\mathbf{R}=\{V \quad \mathcal{Z}\}^T$, $\mathbf{W}=\begin{bmatrix} 1 & 0 \\ 0 & V^{-1} \end{bmatrix}$, and $\Theta=\{V \quad U\}^T$, a linear transformation between $\mathcal{Z}$ and $\Theta=\{V \quad U\}^T$ is realized. According to Eq.(11), one has $|\mathbf{w}|=|v|^{-2}$. Therefore, the PDF of $\mathbf{R}=\{V \quad \mathcal{Z}\}^T$ can be derived based on Eq.(10):

$$p_{\mathbf{R}}(\mathbf{r}) = |v|^{-2} p_{\Theta}(\theta) \tag{12}$$

It is noted that the random vector $\Theta=\{V \quad U\}^T$ can be expressed as a function in terms of V and $\tilde{\mathcal{Z}}=\{1 \quad \mathcal{Z}\}^T$, i.e.:

$$\mathbf{\Theta} = V \begin{Bmatrix} 1 & \dfrac{U}{V} \end{Bmatrix}^T = V\tilde{\mathcal{Z}} \tag{13}$$

By substituting Eq. (13) into (12) leads to the joint PDF of V and $\mathcal{Z}$, i.e., $p_{\mathbf{R}}(\mathbf{r}) = |v|^{-2} p_{\Theta}(v\tilde{z})$. As a result, the PDF of $\mathcal{Z}$ can be easily obtained by marginalizing out the variable V as:

$$p_{\mathcal{Z}}(z) = \int_{\Omega^v} p_{\mathbf{R}}(\mathbf{r}) dv = \int_{\Omega^v} |v|^{-2} p_{\Theta}(v\tilde{z}) dv = \int_{\Omega^{v^{\Re}}} \int_{\Omega^{v^{\Im}}} |v|^2 p_{\Theta}(v\tilde{z}) dv^{\Re} dv^{\Im} \tag{14}$$

where $\tilde{\mathbf{z}}=\{1 \quad \mathbf{z}\}^T$ and $\Omega^{(\bullet)}$ denotes the integration interval of the variable $(\bullet)$.

Based on the formula of $\mathcal{Z}$, one can further calculate the marginal PDFs of the real and imaginary part of $\mathcal{Z}$ by marginalizing out $\mathcal{Z}^{\Im}$ and $\mathcal{Z}^{\Re}$, respectively:

$$p_{\mathcal{Z}^{\Re}}(z^{\Re}) = \int_{\Omega^{v^{\Re}}} \int_{\Omega^{v^{\Re}}} \int_{\Omega^{z^{\Im}}} |v|^2 p_{\Theta}(v\tilde{z}) dv^{\Re} dv^{\Im} dz^{\Im} \tag{15a}$$

$$p_{\mathcal{Z}^{\Im}}(z^{\Im}) = \int_{\Omega^{v^{\Re}}} \int_{\Omega^{v^{\Re}}} \int_{\Omega^{z^{\Re}}} |v|^2 p_{\Theta}(v\tilde{z}) dv^{\Re} dv^{\Im} dz^{\Re} \tag{15b}$$

For a real-valued continuous random variable, the mean is defined as $E(x)=\int_{-\infty}^{\infty} xp(x)dx$ where $p(x)$ is the PDF of x. This definition also holds for more general cases including complex-valued variables. The mean of $\mathcal{Z}^{\Re}$ and $\mathcal{Z}^{\Im}$ can be obtained by integrating $p_{\mathcal{Z}^{\Re}}\left(z^{\Re}\right)$ and $p_{\mathcal{Z}^{\Im}}\left(z^{\Im}\right)$ over the domain of $\mathcal{Z}^{\Re}$ and $\mathcal{Z}^{\Im}$:

$$E\left(z^{\Re}\right)=\int_{\Omega^{z^{\Re}}} z^{\Re} p_{\mathcal{Z}^{\Re}}\left(z^{\Re}\right)dz^{\Re}=\int_{\Omega^{v^{\Re}}}\int_{\Omega^{v^{\Re}}}\int_{\Omega^{z^{\Im}}}\int_{\Omega^{z^{\Re}}} |v|^2 z^{\Re} p_{\Theta}\left(v\tilde{z}\right)dv^{\Re}dv^{\Im}dz^{\Im}dz^{\Re} \tag{16a}$$

$$E\left(z^{\Im}\right)=\int_{\Omega^{z^{\Re}}} z^{\Im} p_{\mathcal{Z}^{\Im}}\left(z^{\Im}\right)dz^{\Im}=\int_{\Omega^{v^{\Re}}}\int_{\Omega^{v^{\Re}}}\int_{\Omega^{z^{\Re}}}\int_{\Omega^{z^{\Im}}} |v|^2 z^{\Im} p_{\Theta}\left(v\tilde{z}\right)dv^{\Re}dv^{\Im}dz^{\Re}dz^{\Im} \tag{16b}$$

Therefore, the unified formula of the PDF of $\mathcal{Z}$, the marginal PDFs of $\mathcal{Z}^{\Im}$ and $\mathcal{Z}^{\Re}$ as well as the statistical moments of $\mathcal{Z}^{\Im}$ and $\mathcal{Z}^{\Re}$ such as the mean can be simply determined by substituting the joint PDF of $\Theta=\{V \quad U\}^T$ into Eq. (14)-(16) and replacing the random vector $\boldsymbol{\Theta}$ by its equivalence $V\tilde{\mathcal{Z}}$.

3 Fast Numerical Solution incorporating SGQ Rule

Whether the closed-form solutions of Eq.(14)-(16) is available or not highly depend on the formula $p_{\Theta}\left(v\tilde{z}\right)$. Obviously, it is non-trivial or impossible to derive the closed-form solutions of $p_{\mathcal{Z}}(z)$ for arbitrary ratio $p_{\Theta}\left(v\tilde{z}\right)$ without following Gaussian distribution, and one should resort to numerical algorithms.

3.1 Gauss quadrature rule

In cases where the integral is univariate, Gaussian quadrature and related approaches are potentially powerful, which is approximated by summing up some items of weighted integrand evaluated at the Gauss points (abscissas) [52,53]:

$$I_1=\int_{\Omega^x} g(x)dx \approx \sum_{i=1}^{n_r} w_i g\left(\tilde{x}_i\right) \tag{17}$$

where n_r is the quadrature order (equal to the number of abscissas), $\tilde{x}_i$ are abscissas (Gauss points), and w_i are weights (Gauss weights); Ω^x denotes the integral region.

The univariate quadrature rule can be extended to multi-dimensional domain by using the product rule, which in turn results in an exponential rise in multivariate quadrature points. The Gauss quadrature formula for a D-dimensional integral is given by [52,53]:

$$I_D = \int_{\Omega^{x_D}} \cdots \int_{\Omega^{x_1}} g\left(x_1, x_2, \cdots, x_D\right) dx_1 \cdots dx_D \approx \sum_{i_D}^{n_{i_D}} \cdots \sum_{i_1=1}^{n_{i_1}} w_{i_1} \cdots w_{i_{i_D}} g\left(\tilde{x}_{i_1}, \tilde{x}_{i_2}, \cdots, \tilde{x}_{i_D}\right) \tag{18}$$

where $\left(n_{i_1} \cdots n_{i_D}\right)$ denote the quadrature order (the number of abscissas) used in $\left(\tilde{x}_1, \tilde{x}_2, \cdots, \tilde{x}_{n_d}\right)$ directions; $\left(\tilde{x}_{i_1}, \tilde{x}_{i_2}, \cdots, \tilde{x}_{i_D}\right)$ are Gauss points; $\left(w_{i_1} \cdots w_{i_{n_d}}\right)$ are the corresponding weights; Ω^{x_i} denotes the integral region of the i-th parameter x_i. It is worth mentioning here that the subscripts involved in 'I' denotes the integral dimension.

3.2 SGQ rule

As is seen from Eq. (18), the total number of points in the Gauss quadrature rule to be calculated increases exponentially with the integral dimension. The curse of dimensionality can hinder the applicability. To address the critical issue, Smolyak-type quadrature formula which is more computationally efficient than the usual multi-dimensional Gauss quadrature rule will be utilized in this study. The Smolyak-type quadrature formula uses Gauss quadrature rule for generating univariate quadrature points and its multi-dimensional extension is obtained using the Smolyak rule [44] utilizing a linear combination of lower-level tensor products of univariate quadrature rules to approximate multivariate integrals. Like the product rule, it combines univariate quadrature rules, so it is very general and easy-implemented. Unlike the product rule, its computational cost does not rise exponentially with the number of considered variables. This gives an additional advantage for SGQ method, i.e. that the accuracy of its estimation can be defined separately.

Definition of quadrature approximation: As indicated in Eq.(17), the one-dimensional quadrature rule delivers the exact value of the integral I_1 if $g(x)$ is a polynomial of a given order. Here we can define a sequence of single-dimension quadrature rules $\Lambda=\{\Lambda_l, l\in\mathbb{N}\}$ so that the order of polynomial increases with the accuracy level l. The quadrature approximation Λ_l is given by [47]:

$$\Lambda_l = \sum_{\tilde{x}\in\mathcal{X}_l} g(\tilde{x})\, w_l(\tilde{x}) \tag{19}$$

Each rule Λ_l specifies n_l nodes $\mathcal{X}_l = \left[\tilde{x}_1, \tilde{x}_2, \cdots, \tilde{x}_{n_l}\right]$ and a corresponding weight function $w_l(\tilde{x})$.

Definition of difference of the quadrature approximation: When increasing the level of accuracy from l-1 to l, the difference of the quadrature approximation is defined as [47]:

$$\Delta_l = \Lambda_l - \Lambda_{l-1} \tag{20}$$

Definition of accuracy level sequences: For the convenience of derivation, a new vector $\boldsymbol{\Xi} \triangleq \{l_1, l_2, \ldots, l_D\}$ is formulated with each of its entries l_i denoting the accuracy level of the univariate-dimensional quadrature rule for the i-th variable. For any nonnegative integer q, the set of accuracy level sequences $\mathbb{N}_q^D$ is defined as [49]:

$$\begin{cases} \mathbb{N}_q^D = \left\{\Xi : \sum_{i=1}^{D} l_i = D + q\right\}, \text{for } q \geq 0 \\ \mathbb{N}_q^D = \varnothing \qquad\qquad\qquad\quad , \text{ for } q < 0 \end{cases} \tag{21}$$

where $\varnothing$ is the empty set; q has the range of $L-D \leq q \leq L-1$. Taking $\mathbb{N}_2^3$ for example, one has $\mathbb{N}_2^3 = \{[1,3],[2,2],[3,1]\}$.

The Smolyak rule: Making full use of the definitions indicated in Eq. (19)-(21), the Smolyak rule states that a numerical approximation with accuracy level $L \in \mathbb{N}$ for D-dimensional integrals denoted by I_D^L can be expressed as [45-49]:

$$I_D^L(g) = \sum_{q=0}^{L-1} \sum_{\Xi \in \mathbb{N}_q^D} \left(\Delta_{l_1} \otimes \Delta_{l_2} \otimes \cdots \otimes \Delta_{l_D} \right)(g) \tag{22}$$

where $\otimes$ stands for the tensor product; the auxiliary parameter q and $\mathbb{N}_q^D$ are defined in Eq.(21).

Wasilkowski et al. [45] proved that Eq. (22) can be explicitly written as

$$I_D^L(g) = \sum_{q=L-D}^{L-1} (-1)^{L-1-q} C_{D-1}^{L-1-q} \sum_{\Xi \in \mathbf{N}_q^D} \left(\Lambda_{l_1} \otimes \Lambda_{l_2} \otimes \cdots \otimes \Lambda_{l_D} \right)(g) \tag{23}$$

where C_{D-1}^{L-1-q} denotes the binomial coefficient with $C_{D-1}^{L-1-q} = \begin{pmatrix} D-1 \\ L-1-q \end{pmatrix}$. By substituting Eq. (18) into Eq.(23) leads to [45]:

$$I_D^L(g) = \sum_{q=L-D}^{L-1} \sum_{\Xi \in \mathbb{N}_q^D} \sum_{\tilde{x}_1 \in \mathcal{X}_{l_1}} \cdots \sum_{\tilde{x}_D \in \mathcal{X}_{l_D}} (-1)^{L-1-q} C_{D-1}^{L-1-q} \times g(\tilde{x}_1, \cdots, \tilde{x}_D) \prod_{i=1}^{D} w_{l_i}(\tilde{x}_i) \tag{24}$$

where $\mathcal{X}_{l_i}$ is the set of quadrature points for single dimension quadrature rule Λ_{l_i}; $[\tilde{x}_1, \cdots, \tilde{x}_D]^T$ is a D-dimensional vector of SGQ points where $\tilde{x}_j \in \mathcal{X}_{l_j}$; $w_{l_i}(\tilde{x}_i)$ are the weight in Λ_{l_i} associated with $\tilde{x}_j \in \mathcal{X}_{l_j}$. Eq. (24) boils down to a weighted sum of function evaluations $f(\mathbf{x})$.

The sets of nodes $[\tilde{x}_1, \cdots, \tilde{x}_D]^T$ are determined by the relevant combinations of nodes of univariate quadrature rules Λ_{l_i}, where the levels of accuracy in each dimension are determined by $\Xi \in \mathbb{N}_q^D$ and $L - D \le q \le L-1$. The corresponding weights are $(-1)^{L-1-q} C_{D-1}^{L-1-q} \prod_{i=1}^{D} w_{l_i}(\tilde{x}_i)$. The final set of the SGQ points are given as [49]:

$$\mathcal{X}_D^L = \bigcup_{q=L-D}^{L-1} \bigcup_{\Xi \in \mathbb{N}_q^D} \left(\mathcal{X}_{l_1} \otimes \mathcal{X}_{l_2}, \cdots \otimes \mathcal{X}_{l_D} \right) \tag{25}$$

where $\bigcup(\bullet)$ represents union of the individual SGQ points. The procedures of generating points and weights from the univariate quadrature point sets using the Smolyak rule are shown in Table 1. The MATLAB implementation of the SGQ algorithm is referred to the Appendix of [54]. The quadrature points required to be generated for conventional Gaussian quadrate rule [55] and SGQ rule are compared in Table 2, which clearly shows that the SGQ rule can reduce the quadrature points, thus improving the computation efficiency significantly.

Table 1: The algorithm of generating SGQ points and weights [49]

Input: dimension D, accuracy level L **Output**: matrix χ containing the SGQ nodes with the element of χ_i, vector W containing the respective weights with the element of W_i;	
Step 1	FOR $l=1:L$ ● Select the quadrature point set of the univariate Gaussian quadrature rule Λ_{l_i} and the corresponding weight w_{l_i}; ● Determine $\mathcal{X}_{l_1}, \mathcal{X}_{l_2}, \cdots, \mathcal{X}_{l_D}$ and the corresponding weights of the points; END

Step 2	FOR $q = L-D : L-1$
	● Determine $\mathbb{N}_q^n$ following the equation: $\sum_{i=1}^{D} l_i = D+q$ with $1 \le l_i < n+q$
	FOR each element of $\Xi \triangleq \{l_1, l_2, \ldots, l_D\}$ in $\mathbb{N}_q^n$
	➢ Form $\left(\mathcal{X}_{l_1} \otimes \mathcal{X}_{l_2}, \cdots \otimes \mathcal{X}_{l_D}\right)$;
	FOR each point $[x_1, \cdots, x_D]^T \left(x_i \in \mathcal{X}_{l_i}\right)$ in $\left(\mathcal{X}_{l_1} \otimes \mathcal{X}_{l_2} \cdots \otimes \mathcal{X}_{l_D}\right)$
	IF the point is new
	✧ Add the point to χ;
	✧ Assign a new index i to this point;
	✧ Set the weights of χ_i as $W_i = (-1)^{L-1-q} C_{n-1}^{L-1-q} \prod_{j=1}^{n} \hat{w}_{s_j} \left(\hat{w}_{s_j} \in \hat{w}\right)$;
	ELSE (the points already exists)
	✧ Update the weight by $W_i = W_i + (-1)^{L-1-q} C_{n-1}^{L-1-q} \prod_{j=1}^{n} \hat{w}_{s_j} \left(\hat{w}_{s_j} \in \hat{w}\right)$;
	END IF
	END FOR
	END FOR
	END FOR

Table 2: The number of quadrature points required by two quadrature rules under consideration

Integral dimension n	Accuracy level L	Number of quadrature points	
		Gaussian quadrature	SGQ
2	3	49	17
	4	169	45
	5	441	97
3	3	343	35
	4	2197	105
	5	9261	297
4	3	2401	55
	4	28561	207
	5	194481	681

3.3 Summary of procedures

The main procedures for calculating the PDF of arbitrary complex-valued ratio distribution using the unified scheme are summarized in Table 3.

Table 3: The procedures of calculating the PDF of complex-valued ratio distribution with the unified scheme

Step	Procedures
1	Formulate $p_{\Theta}(v\tilde{z})$ through replacing Θ by $V\tilde{\mathcal{Z}}$
2	Formulate the unified formula by substituting $p_{\Theta}(v\tilde{z})$ into (14)-(16)
3	Generate SGQ points and weights following the algorithm in Table 1
4	Calculate the multi-dimensional integral involved in (14)-(16) by using Eq. (24) based on the SGQ points and weights

4 Applications to Statistical Inference for FRF and TF

4.1 Definition of FRF and TF

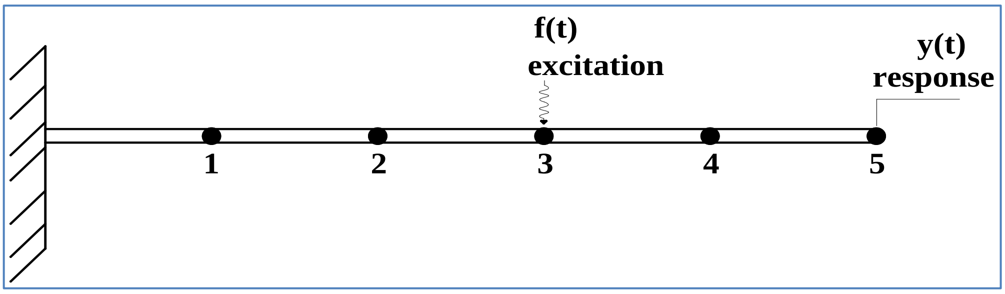

Fig. 1: Typical diagram of a dynamic system subject to a single input

Of interest now are problems involving a single-input dynamical system shown in Fig.1. For a multi-degree-of-freedom (MDOF) linear system, it is assumed that a single input is applied on the i-th DOF, and the response measurements are available for n_o measured DOFs. The time history can be modeled as a realization of stochastic vector process, which is denoted by $f_i(t)$ and $\mathbf{y}(t)=\left\{y_0(t), y_1(t),\cdots, y_{n_o}(t)\right\}^T$ for the input and output, respectively. The corresponding discrete-time stochastic vector processes of $f_i(t)$ and $y_j(t)$ are denoted by $f_i(n)=\left\{f_i(0), f_i(\Delta t),\cdots, f_i((N-1)\Delta t)\right\}^T$ and $y_j(n)=\left\{y_j(0), y_j(\Delta t),\cdots, y_j((N-1)\Delta t)\right\}^T$, which correspond to the sampled data in real applications. At frequency ω_k, the discrete Fourier transforms of the input and output measures are defined as:

$$\begin{cases} F_i^{(\omega_k)} = F_i^{\Re}(\omega_k) + \mathbf{i}F_i^{\Im}(\omega_k) = \sqrt{\Delta t/2\pi N}\sum_{n'=0}^{N-1} f_i(n)e^{(-\mathrm{i}\omega_k n\Delta t)} \\ Y_j^{(\omega_k)} = Y_j^{\Re}(\omega_k) + \mathrm{i}Y_j^{\Im}(\omega_k) = \sqrt{\Delta t/2\pi N}\sum_{n'=0}^{N-1} y_j(n)e^{(-\mathrm{i}\omega_k n\Delta t)} \end{cases} \tag{26}$$

where $\mathrm{i}^2=-1$, $\omega_k = 2\pi f_k$, $k=1,2,\cdots,Int(N/2)$, and $\Delta\omega = 2\pi/(N\Delta t)$. In this work, '$\omega_k$' shown in a bracket or superscript denotes the frequency point.

As a result, the FRF $H_{ij}^{(\omega_k)}$ reflecting the input-output relationship between $f_i(t)$ and $y_j(t)$, as well as TF $T_{ij}^{(\omega_k)}$ reflecting the output-output relationship between an arbitrary response $Y_j^{(\omega_k)}$ and a reference response $Y_i^{(\omega_k)}$ are defined as:

$$H_{ij}^{(\omega_k)} = Y_j^{(\omega_k)} \Big/ F_i^{(\omega_k)} \tag{27a}$$

$$T_{ij}(\omega_k) = Y_j^{(\omega_k)} \Big/ Y_i^{(\omega_k)} \tag{27b}$$

As seen from Eq.(27a) and (27b), both FRF and TF are complex-valued ratio random variables composed of both real and imaginary parts which are correlated with each other. As emphasized frequently, one of the core issues in developing probabilistic models for raw FRFs and TFs is to investigate the statistics of the frequency-domain stochastic vector of the input and output, i.e., $\Psi_k = \left[F_i^{(\omega_k)}, Y_j^{(\omega_k)}\right]$ or $\Psi_k = \left[Y_i^{(\omega_k)}, Y_j^{(\omega_k)}\right]$.

4.2 Probabilistic models of FFT coefficients in the complex domain

It is worth mentioning here that this study concerns FRFs and TFs defined as the ratio of raw FFT coefficient of two responses without resorting to any post-processing such as averaging, smoothing and windowing as raw FFT coefficients provide a one-to-one relationship between the time-domain data and its frequency domain information [56-58]. The statistics of the raw FFT coefficients have been studied extensively over the past few decades [59-63]. One can propose different probabilistic models to quantify the uncertainty of FFT coefficients, and the performance of different probabilistic models may be dependent on the nature of excitation, the length of time history, etc. Here, two probabilistic models including the complex Gaussian distribution [61-63] and complex-valued t distribution [43] will be used to model joint PDF of two FFT coefficients.

A Gaussian probabilistic model has been utilized to model the uncertainty of the FFT coefficients due to the additive noise disturbance during the measurement process [61,62]. Gaussian probabilistic model states that, for the FFT random vector $\Psi_k = \left[F_i^{(\omega_k)}, Y_j^{(\omega_k)}\right]$ or $\Psi_k = \left[Y_i^{(\omega_k)}, Y_j^{(\omega_k)}\right]$, $\Psi_k^{\Re}$ and $\Psi_k^{\Im}$ are Gaussian distributed as the number of discrete-time points

$N \to \infty$ according to the central limit theorem, and the PDF of the complex random vector Ψ_k is given by [61-63]:

$$p_{\boldsymbol{\varphi}_k}\left(\boldsymbol{\Psi}_k\right) = \frac{1}{\pi^{n_o}\left|\det \boldsymbol{\Sigma}_k\right|} e^{-\boldsymbol{\varphi}_k^* \boldsymbol{\Sigma}_k^{-1} \boldsymbol{\varphi}_k} \tag{28}$$

where $\boldsymbol{\varphi}_k$ denotes the value of the random vector $\boldsymbol{\Psi}_k$; the covariance matrix of $\boldsymbol{\Psi}_k$ is given by [61-63]:

$$\boldsymbol{\Sigma}_k = \mathbf{G}_k^{\Re} + \mathbf{i}\mathbf{G}_k^{\Im} \tag{29}$$

where $\mathbf{G}_k = E\left(\boldsymbol{\Psi}_k \boldsymbol{\Psi}_k^*\right)$ denotes the mathematical expectation of the raw PSD matrix of $\boldsymbol{\Psi}_k$.

Recent study reveals that the complex Gaussian distribution is tilted towards certain FFT coefficients, while complex-valued t distribution offers a more viable alternative with respect to FFT coefficients at other frequencies, particularly because its peaks and tails are more realistic. Given that Ψ_k follows a complex-valued t distribution, then the PDF is given by [43]:

$$p_{\boldsymbol{\Psi}_k}\left(\boldsymbol{\varphi}_k\right) = \frac{1}{\left(\pi/2\right)^{n_o} C\left(\vartheta, 2n_o\right)\left|\boldsymbol{\Xi}_k\right|}\left(1 + \frac{2}{\vartheta}\boldsymbol{\varphi}_k^* \boldsymbol{\Xi}_k^{-1} \boldsymbol{\varphi}_k\right)^{-\left(\vartheta + 2n_o\right)/2} \tag{30}$$

where ϑ is the shape parameter of t distribution, also known as the DOF of statistics; $\boldsymbol{\Xi}_k = \frac{\vartheta - 2}{\vartheta}\boldsymbol{\Sigma}_k$.

4.3 Statistical inference for FRF and TF

In the context of statistical inference for FRF and TFs, the integral interval of the FFT coefficients are $[-\infty, +\infty]$. Therefore, the PDF of $\mathcal{Z}$, the marginal PDF of $\mathcal{Z}^{\Re}$ and $\mathcal{Z}^{\Im}$, as well as the expected values of $\mathcal{Z}^{\Re}$ and $\mathcal{Z}^{\Im}$ are given by:

$$p_{\mathcal{Z}}\left(z\right) = \int_{-\infty}^{+\infty}\int_{-\infty}^{+\infty} \left|v\right|^2 p_{\Theta}\left(v\tilde{z}\right) dv^{\Re} dv^{\Im} \tag{31a}$$

$$p_{\mathcal{Z}^{\Re}}\left(z^{\Re}\right) = \int_{-\infty}^{+\infty}\int_{-\infty}^{+\infty}\int_{-\infty}^{+\infty} \left|v\right|^2 p_{\Theta}\left(v\tilde{z}\right) dv^{\Re} dv^{\Im} dz^{\Im} \tag{31b}$$

$$p_{\mathcal{Z}^{\Im}}\left(z^{\Im}\right) = \int_{-\infty}^{+\infty}\int_{-\infty}^{+\infty}\int_{-\infty}^{+\infty} \left|v\right|^2 p_{\Theta}\left(v\tilde{z}\right) dv^{\Re} dv^{\Im} dz^{\Re} \tag{31c}$$

$$E\left(z^{\Re}\right)=\int_{-\infty}^{+\infty}\int_{-\infty}^{+\infty}\int_{-\infty}^{+\infty}\int_{-\infty}^{+\infty}|v|^2\, z^{\Re}\, p_{\Theta}\left(v\tilde{z}\right)dv^{\Re}dv^{\Im}dz^{\Im}dz^{\Re} \tag{31d}$$

$$E\left(z^{\Im}\right)=\int_{-\infty}^{+\infty}\int_{-\infty}^{+\infty}\int_{-\infty}^{+\infty}\int_{-\infty}^{+\infty}|v|^2\, z^{\Im}\, p_{\Theta}\left(v\tilde{z}\right)dv^{\Re}dv^{\Im}dz^{\Re}dz^{\Im} \tag{31e}$$

where $\tilde{\mathbf{z}}=\{1 \quad \mathbf{z}\}^T$.

Given the probabilistic models of $\Psi_k=\left[F_i^{(\omega_k)},Y_j^{(\omega_k)}\right]$ and $\Psi_k=\left[Y_i^{(\omega_k)},Y_j^{(\omega_k)}\right]$, we can determine the PDF of FRF and TF using Eq.(31) by replacing the general mathematical symbols as follows:

- For FRF: $\Theta=\Psi_k=\left[F_i^{(\omega_k)},Y_j^{(\omega_k)}\right]$; $\mathcal{Z}=H_{ij}^{(\omega_k)}$; $\tilde{\mathcal{Z}}=\left[1, H_{ij}^{(\omega_k)}\right]^T$; $V=F_i^{(\omega_k)}$; $V\tilde{\mathcal{Z}}=F_i^{(\omega_k)}\left[1,H_{ij}^{(\omega_k)}\right]$.
- For TF: $\Theta=\Psi_k=\left[Y_i^{(\omega_k)},Y_j^{(\omega_k)}\right]$; $\mathcal{Z}=T_{ij}^{(\omega_k)}$; $\tilde{\mathcal{Z}}=\left[1, T_{ij}^{(\omega_k)}\right]^T$; $V=Y_i^{(\omega_k)}$; $V\tilde{\mathcal{Z}}=Y_i^{(\omega_k)}\left[1,T_{ij}^{(\omega_k)}\right]$.

As a result, we can use the SGQ rule introduced in Section 3 to solve the PDF of $\mathcal{Z}$ as well as its extensions. The procedures for computing the PDF for FRFs are summarized in Table 4, which can be easily extended to the statistical inference for TF.

Table 4: Statistical inference for FRF using the unified scheme

Step	Procedures
1	Take FFT for different sets of time histories $\Psi_k=\left[F_i^{(\omega_k)},Y_j^{(\omega_k)}\right]$;
2	Calculate the covariance of the FFT samples of different measurements $\mathbf{\Sigma}_k=\mathbf{G}_k^{\Re}+\mathbf{i}\mathbf{G}_k^{\Im}$ with $\mathbf{G}_k=E\left(\mathbf{\Psi}_k\mathbf{\Psi}_k^*\right)$;
3	FOR $k=k_1:k_2$ ● Select the probabilistic model for FFT coefficients $p_{\Psi_k}\left(\varphi_k\right)$ at ω_k; ● Formulate $p_{\Theta}\left(v\tilde{z}\right)$ by setting $\Theta=\Psi_k=\left[F_i^{(\omega_k)},Y_j^{(\omega_k)}\right]$, $\mathcal{Z}=H_{ij}^{(\omega_k)}$, $\tilde{\mathcal{Z}}=\left[1, H_{ij}^{(\omega_k)}\right]^T$, $V=F_i^{(\omega_k)}$ and $V\tilde{\mathcal{Z}}=F_i^{(\omega_k)}\left[1,H_{ij}^{(\omega_k)}\right]$; ● Formulate the unified formula by substituting $p_{\Theta}\left(v\tilde{z}\right)$ into (31); ● Generate SGQ points and weights for $V^{\Re}$, $V^{\Im}$, $\mathcal{Z}^{\Re}$ and $\mathcal{Z}^{\Im}$ by following Table 1; ● Calculate multiple integrals in Eq. (31) following the Table 3. END FOR

5 Case Studies

5.1 Vibration testing of a simply supported beam

To illustrate the efficiency of the proposed methodology of this study, the theoretical findings are validated with tests on a simply supported beam shown in Fig. 2. The length of the beam is 3 m, while its cross-section is $0.1\ \mathrm{m} \times 0.02\ \mathrm{m}$. The beam was subject to hammer excitation. The input force and output acceleration were measured simultaneously with a sampling frequency of $200\ \mathrm{Hz}$. Five sensors were set directly on the beam. The arrangement of the acceleration sensors and measurement points are shown in Fig. 2(a). The DH5981 Dynamic Signal Test Analysis System, the impact hammer (type LC02) and a laptop were employed in the field test. The DH5981 Dynamic Signal Test Analysis System and the impact hammer were produced by Donghua Testing Company in China. The experimental setup is shown in Fig. 2(b).

To verify the proposed probabilistic models, the response measurements are segmented into 200 non-overlapping sequences with each one lasting 120 s. The FFT coefficients were then calculated for each realization to formulate samples of the FRFs and TFs at different frequency points. The raw FFT coefficients without any post-processing such as averaging, smoothing and windowing is used to verify the proposed algorithm. As a result, a thorough validation can be implemented in a similar way to Monto Carlo simulation (MCS) with each segment viewed as a random realization.

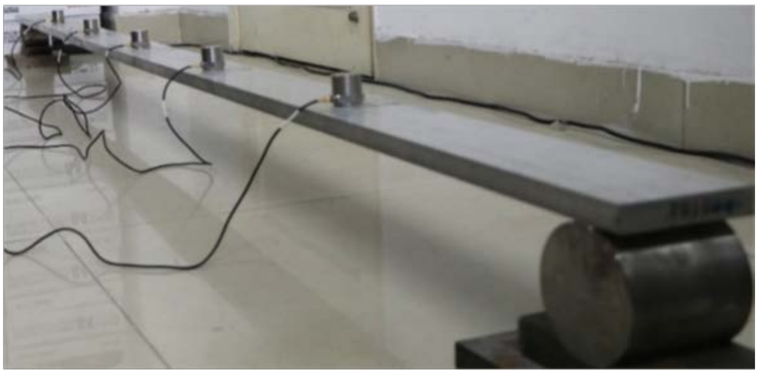

(a)

(b)

Fig. 2: The tested simply supported beam (a) and experimental setup (b)

5.1.1 The K-S test of FFT coefficients

The K-S test was conducted by comparing the distribution of the samples (i.e., the FFT coefficients) with an assumed distribution for the real and the imaginary parts within the frequency band [0,10] Hz. When the K-S test is equal to 0, the FFT coefficients follow the assumed distribution; when the K-S test is equal to 1, the corresponding probability model and the assumption should be rejected. The K-S test results by assuming that the real and imaginary parts of FFT coefficients of $F_1^{(\omega_k)}$ and $Y_1^{(\omega_k)}$ follow a Gaussian distribution are shown in Fig. 3(a), which indicates that the complex Gaussian distribution can model the distributions of FFT coefficients at a set of frequencies successfully. However, the test data analysis also emphasizes the existence of non-Gaussianity, especially for the excitation. The K-S test results, by assuming that the real and imaginary parts of FFT coefficients of $Y_1^{(\omega_k)}$ follow a t distribution, are shown in Fig. 3(b). By comparing Fig. 3(a) and (b), the passing rates of the t-distribution are significantly higher than that of the Gaussian distribution.

Fig. 4(a) and (b) shows the probability plots of $Y_1^{(\omega_k)}$ at $\omega_k = 8.28\pi$ rad/s and $\omega_k = 0.18\pi$ rad/s . Scattered samples were compared with a straight line to judge the fitting quality of the Gaussian distribution. The circles in the probability plot denote the empirical probability versus the data value for each point in the sample. For Fig. 4(a), the markers lie on a curve that coincides with the straight red line, indicating that the Gaussian assumption was proper for the given samples. However, the scattered samples of $Y_1^{(\omega_k)}$ at ω_k =0.18π rad/s shown in Fig. 4(b) were S-shaped, indicating that the t location-scale probability plot better fits the samples, accounting for the heavy tails. Therefore, a complex Gaussian probabilistic model and complex t probabilistic model will be used to model FFT coefficients at different frequencies, which will be further used to infer the statistical distribution of FRF and TF.

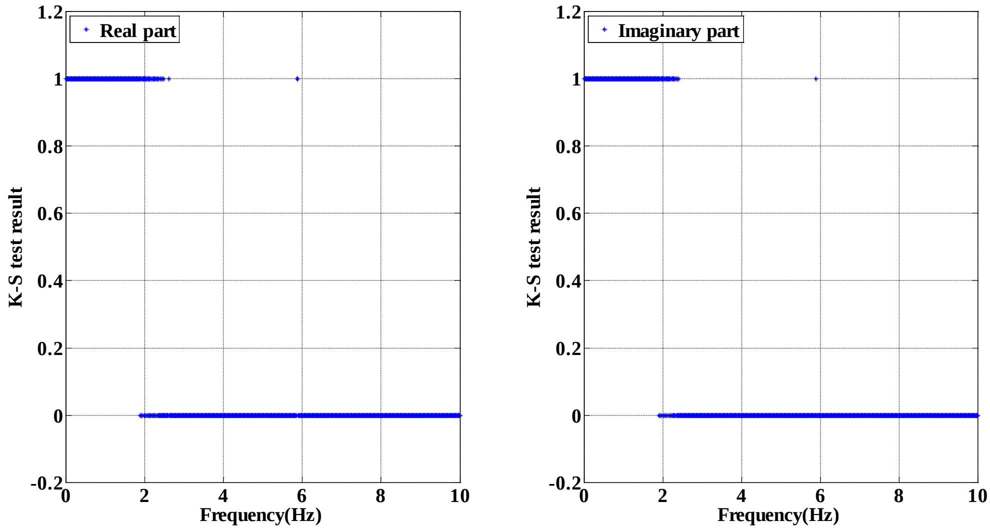

(a) The real (left) and imaginary parts (right) of $Y_1^{(\omega_k)}$ by assuming the Gaussian distribution

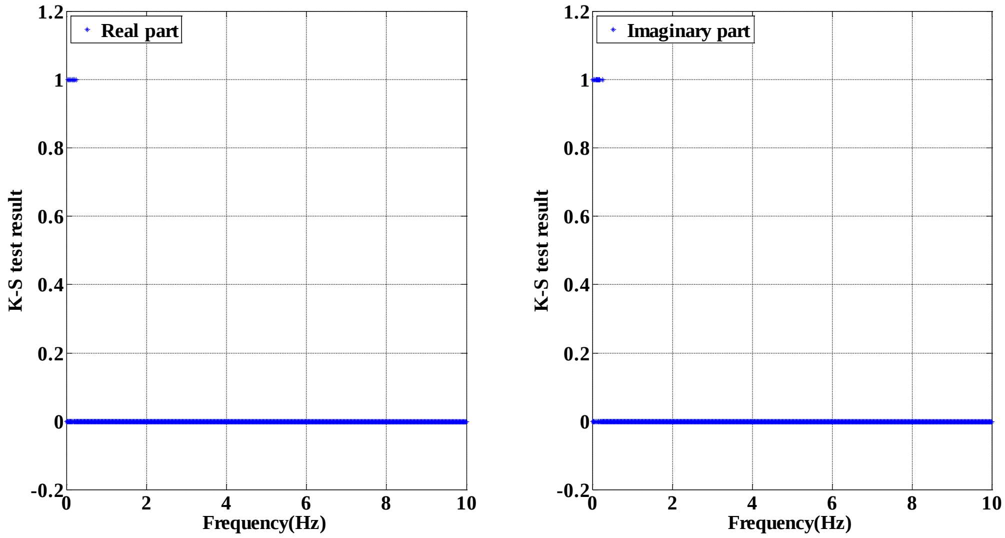

(b) The real (left) and imaginary parts (right) of $Y_1^{(\omega_k)}$ by assuming t distribution

Fig. 3: K-S test of the real and imaginary parts of FFT coefficients of $Y_1^{(\omega_k)}$: comparing the distribution of the samples with (a) Gaussian distribution and (b) t distribution

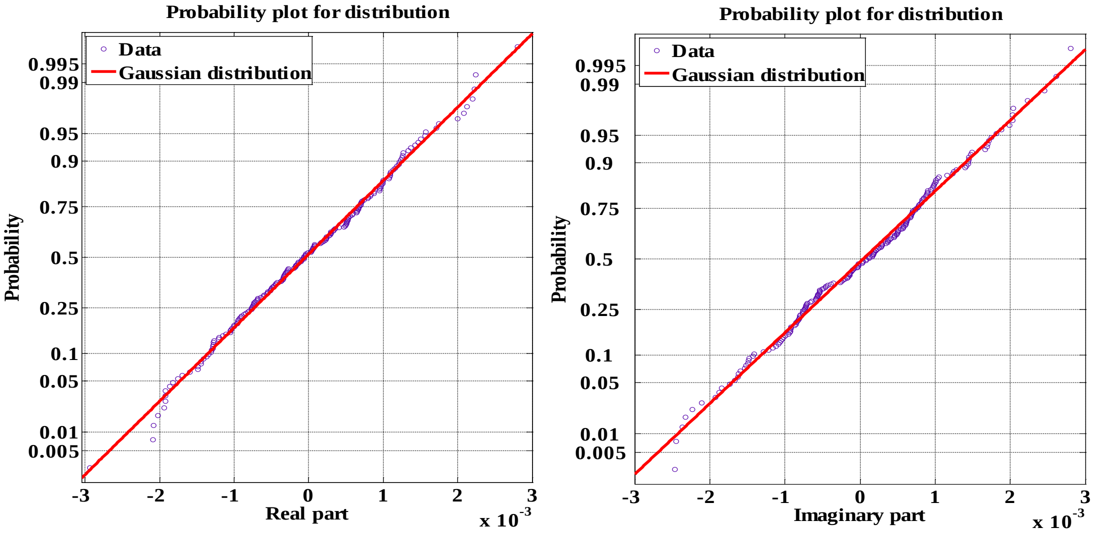

(a) Probability plots at ω_k =8.28π rad/s

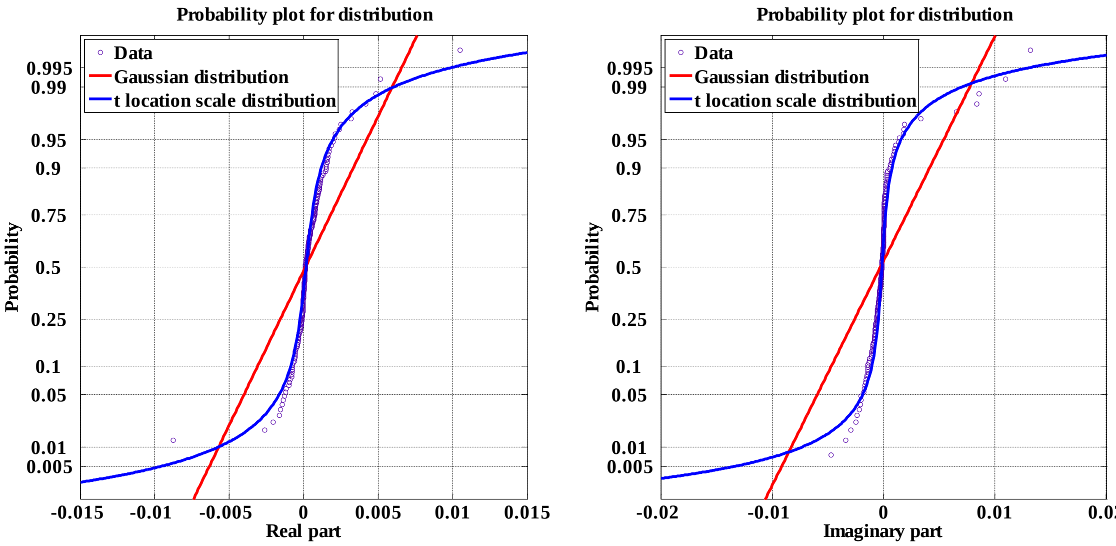

(b) Probability plots at ω_k =0.18π rad/s

Fig. 4: Probability plots of the real and the imaginary parts of $Y_1^{(\omega_k)}$ at ω_k =8.28π rad/s and ω_k =0.18π rad/s

5.1.2 Statistical inference for FRFs

The distribution properties of the FRF $H_{15}^{(\omega_k)}$ at $\omega_k = 8.28\pi\,\text{rad/s}$, the denominator and nominator of which pass the K-S test, were observed. At the frequency line $\omega_k = 8.28\pi\,\text{rad/s}$, the K-S test shows that it follows a Gaussian distribution. Here, the FRF can be modelled by a univariate circularly-symmetric complex Gaussian ratio distribution, the closed-form formula of which was derived in [19]. By denoting the covariance matrix of $\left[F_1^{(\omega_k)}, Y_5^{(\omega_k)}\right]$ as $\mathbf{\Sigma} = \begin{bmatrix} \sigma_0^2 & \rho\sigma_0\sigma_1 \\ \rho^*\sigma_0\sigma_1 & \sigma_1^2 \end{bmatrix}$, where $\rho = \rho^{\Re} + \mathbf{i}\rho^{\Im}$ denotes the complex correlation coefficient, the analytical formulas of $p_{\mathcal{Z}}(z)$, $p_{\mathcal{Z}^{\Re}}\left(z^{\Re}\right)$, and $p_{\mathcal{Z}^{\Im}}\left(z^{\Im}\right)$ are given by:

$$p_{\mathcal{Z}}(z) = \pi^{-1}\left(1-\rho^*\rho\right)\sigma_0^2\sigma_1^2\left[\sigma_1^2 - \left(z^*\rho^* + z\rho\right)\sigma_0\sigma_1 + zz^*\sigma_0^2\right]^{-2} \tag{32a}$$

$$p_{\mathcal{Z}^{\Re}}\left(z^{\Re}\right) = \frac{(1-|\rho|^2)\sigma_0^4\sigma_1^2}{2\sqrt{[-2\sigma_0^3\sigma_1\rho^{\Re}z^{\Re} + \sigma_0^4\left(z^{\Re}\right)^2 + \sigma_0^2\sigma_1^2(1-\left(\rho^{\Im}\right)^2)]^3}} \tag{32b}$$

$$p_{\mathcal{Z}^{\Im}}\left(z^{\Im}\right) = \frac{(1-|\rho|^2)\sigma_0^4\sigma_1^2}{2\sqrt{(2\sigma_0^3\sigma_1\rho^{\Im}z^{\Im} + \sigma_0^4(z^{\Im})^2 + \sigma_0^2\sigma_1^2(1-(\rho^{\Re})^2))^3}} \tag{32c}$$

Fig. 5 compares the theoretical curves of the real and imaginary parts of $H_{15}^{(\omega_k)}$ (i.e., Eq. (32b) and (32c)), denoted by dotted lines, with the probability mass functions represented by histograms drawn from all the samples. For the purpose of comparison, the PDF of $H_{15}^{(\omega_k)}$ was also calculated using the SGQ algorithm introduced in Section 3 and plotted in Fig. 5 by solid lines. As is seen in Fig. 5, the curve achieved using the numerical algorithm coincides with the closed-form formula (32), both of which can fit the histograms well. Therefore, the unified scheme for solving the complex-valued ratio distribution can achieve satisfactory results.

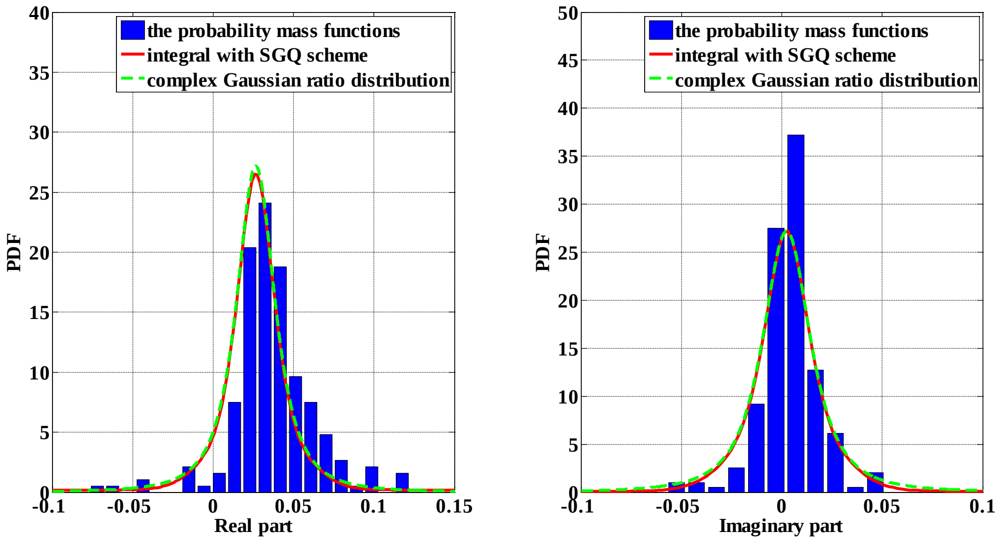

Fig. 5: Comparison of the marginal PDFs calculated using the analytical formula [Eq. (32)] and numerical method, as well as the histogram of the real part and imaginary parts of $H_{15}^{(\omega_k)}$ at ω_k =8.28π rad/s

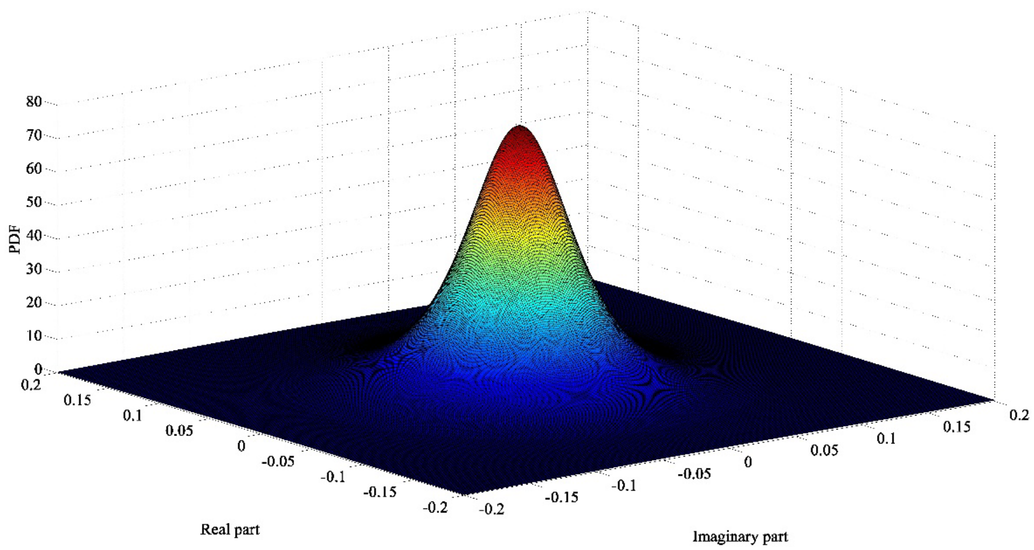

Fig. 6: The 3D-shaded surface plot of the joint PDF of the real and imaginary parts of $H_{15}^{(\omega_k)}$ at ω_k =0.18π rad/s

To further illustrate the efficiency of the unified approach, the distribution properties of $H_{15}^{(\omega_k)}$ at ω_k =0.18π rad/s were also observed. The FFT coefficients $F_1^{(\omega_k)}$ and $Y_5^{(\omega_k)}$ at ω_k =0.18π rad/s were modelled using a complex-valued t distribution. The variance of $F_1^{(\omega_k)}$

and $Y_5^{(\omega_k)}$ are equal to 0.0679 and 0.0062, respectively, while their complex correlation coefficient is equal to $0.1907-0.0228i$. For $F_1^{(\omega_k)}$ and $Y_5^{(\omega_k)}$, the shape parameters of the t distribution are set as 9 and 3, respectively. The random variable $H_{15}^{(\omega_k)}$ at ω_k =0.18π rad/s was modelled using a complex t ratio distribution, the PDF of which was computed by following the procedures in Table 4. Fig. 6 shows the 3D-shaded surface plot of the joint PDF of the real and imaginary parts of $H_{15}^{(\omega_k)}$ at ω_k =0.18π rad/s . In Fig. 7, the solid and dotted lines denote the PDFs ω_k =0.18π rad/s computed with the proposed numerical algorithm and those of the circularly-symmetric complex Gaussian ratio distribution, respectively, while the histograms denote the probability mass functions achieved from the FFT samples. The comparison shown in Fig. 7 indicates that the t ratio distribution can be computed with high accuracy using the numerical algorithm, and its performance is better than that of the complex Gaussian distribution at ω_k =0.18π rad/s .

The complex t ratio distribution of the real and imaginary parts of $H_{15}^{(\omega_k)}$ at ω_k =0.18π rad/s computed using SGQ rule with 1320 quadrature points as well as those calculated using Gaussian quadrature rule with 1331 and 9261 quadrature points are compared in Fig. 7(b). The complex t ratio distribution computed with the SGQ rule is denoted by the solid line, while the PDF computed using Gaussian quadrature rule with 1331 and 9261 quadrature points are denoted by yellow dashed line and green dashed line, respectively. As is seen from Fig.7(b), the SGQ rule can achieve high accuracy when only 1320 quadrature points are used, while the results computed using Gaussian quadrature rule with similar number of quadratic points have much poorer performance. With the increase of the quadrature points, the accuracy of the results computed using the Gaussian quadrature rule approach those computed using the SGQ rule. Table 5 shows the time consumption of computing the PDF of $H_{15}^{(\omega_k)}$, the marginal PDF of $\left[H_{15}^{(\omega_k)}\right]^{\Re}$, and the mean of $\left[H_{15}^{(\omega_k)}\right]^{\Re}$ at ω_k=0.18π rad/s by the using Gaussian quadrature rule and SGQ rule introduced in Section 3. From Table 5, it can be concluded that the time consumed by the proposed numerical scheme of employing sparse-grid theory is reduced significantly. Therefore, the unified solution is expected to be efficient in quantifying the uncertainties of FRF when it is non-trivial or impossible to discover its closed-form solution due to the complexity of multi-dimensional integrals.

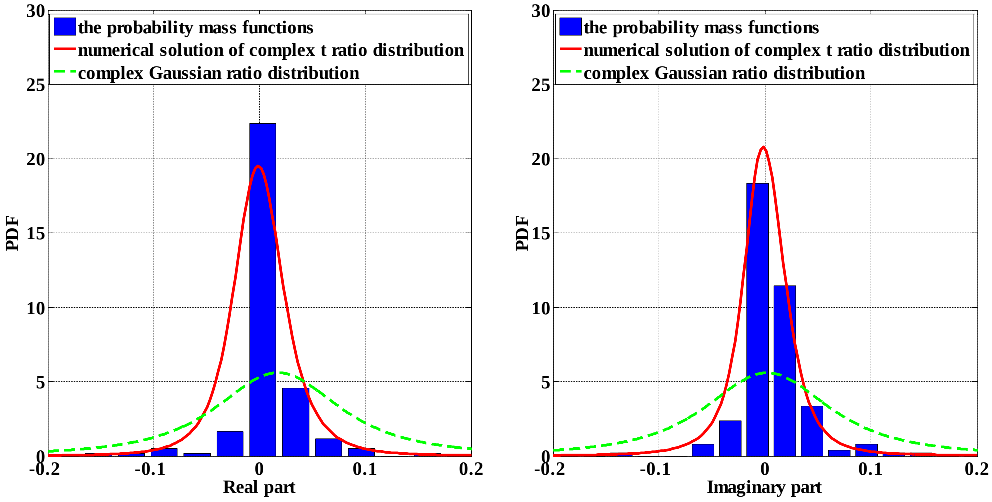

(a) Comparison of the probability mass function, the complex t ratio distribution computed using SGQ rule and the complex Gaussian ratio distribution

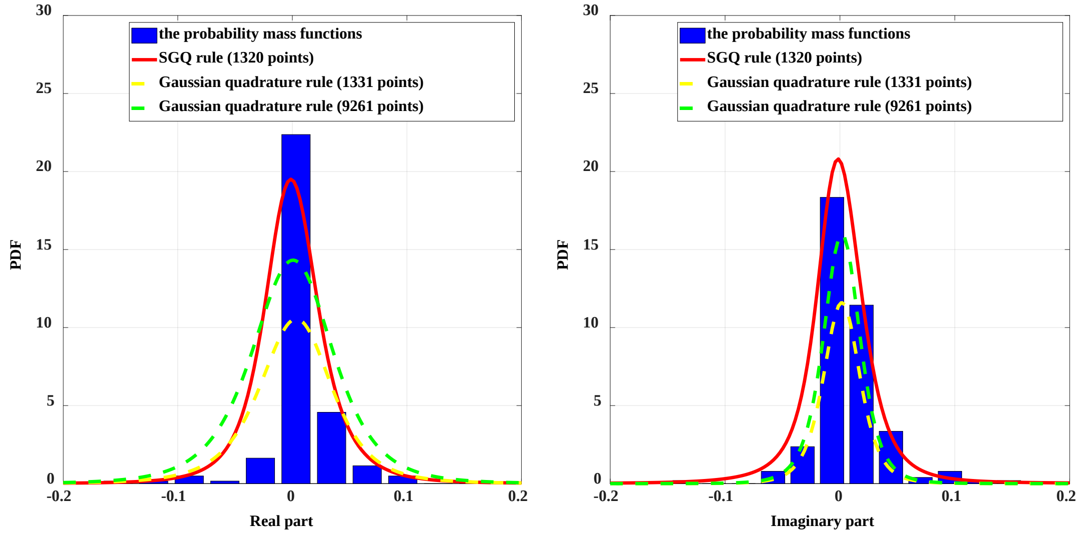

(b) Comparison of the numerical solution of complex t ratio distribution computed using SGQ rule (1320 quadrature points) and Quadratic rule (1331 and 9261 quadrature points)

Fig. 7: The marginal PDFs and histogram of the real and imaginary parts of $H_{15}^{(\omega_k)}$ at $\omega_k = 0.18\pi$ rad/s

Table 5: Time consumed by two different numerical strategies for the simply supported beam

Items	PDFs	Gaussian quadrature		Sparse-grid quadrature	
		Time (s)	Quadrature points	Time (s)	Quadrature points
FRF at $\omega_k = 0.18\pi$ rad/s	PDF of $H_{15}^{(\omega_k)}$	62.87	441	6.85	377
	Marginal PDF of $\left[H_{15}^{(\omega_k)}\right]^{\Re}$	493.04	9261	18.11	1320
	Expectation of $\left[H_{15}^{(\omega_k)}\right]^{\Re}$	7086.75	194481	19.35	4433
TF at $\omega_k = 4.31\pi$ rad/s	PDF of $T_{15}^{(\omega_k)}$	65.72	441	7.16	377
	Marginal PDF of $\left[T_{15}^{(\omega_k)}\right]^{\Re}$	486.23	9261	17.86	1320
	Expectation of $\left[T_{15}^{(\omega_k)}\right]^{\Re}$	6368.92	194481	17.39	4433

5.1.3 Statistical inference for TFs

To illustrate the applicability of the proposed unified solution of complex ratio distribution, the performance of TFs is observed here. The TF corresponding to the fifth sensor and the first sensor (i.e., $T_{15}^{(\omega_k)}$) is considered first at the frequency line $\omega_k = 4.31\pi$ rad/s . The variances of $Y_1^{(\omega_k)}$ and $Y_5^{(\omega_k)}$ are equal to 7.3587×10^{-5} and 7.6863×10^{-5}, respectively, and their complex correlation coefficient is equal to $0.7047+0.0244i$. The K-S test result indicates that $T_{15}^{(\omega_k)}$ at $\omega_k = 4.31\pi$ rad/s follows a complex t ratio distribution. Following the procedures demonstrated in Table 4, the unified formula of the PDF of $T_{15}^{(\omega_k)}$ can be determined according to Eq. (31), which was then solved numerically by using the SGQ rule introduced in Section 3. The 3Dshaded surface plot of the joint PDF of the real and imaginary parts of $T_{15}^{(\omega_k)}$ is presented in Fig. 8.

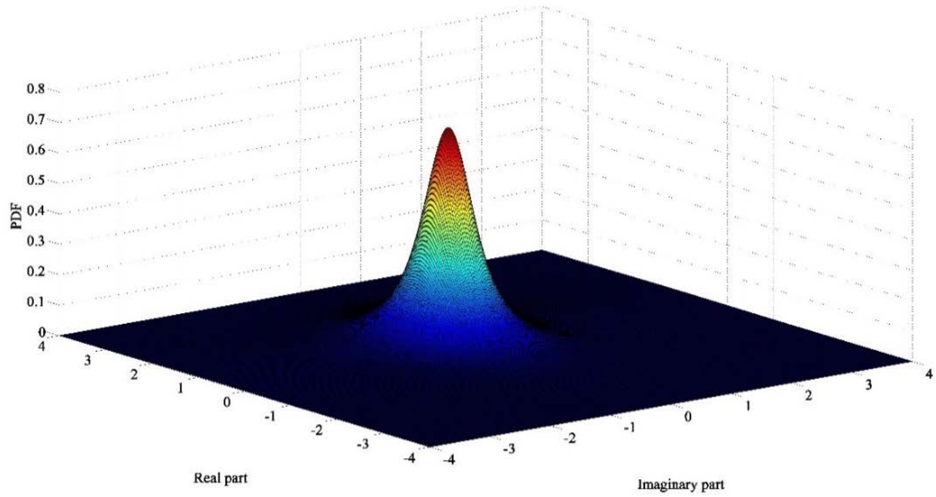

Fig. 8: The 3D-shaded surface plot of the joint PDF of the real and imaginary parts of $T_{15}^{(\omega_k)}$ at ω_k=4.31π rad/s

In Fig. 9, the solid line denotes the theoretical PDFs of the real and imaginary parts of $T_{15}^{(\omega_k)}$, while the histograms denote the probability mass functions drawn from 200 samples. As seen from Fig. 9, there is a good consistency between the observed histograms and the PDF of the complex t ratio distribution that was calculated using the SGQ rule. The PDF of the real and imaginary parts of $T_{15}^{(\omega_k)}$ computed using SGQ rule as well as those calculated using Gaussian quadrature rule are compared in Fig. 9(b). As is seen from Fig.9(b), Gaussian quadrature rule should involve significantly more quadrature points to achieve similar accuracy to those of SGQ rule involving only 1320 quadrature points. The time required for computing the PDF of $T_{15}^{(\omega_k)}$, the marginal PDF of $\left[T_{15}^{(\omega_k)}\right]^{\Re}$, as well as the expected value of $\left[T_{15}^{(\omega_k)}\right]^{\Re}$ at ω_k=4.31π rad/s by the Gaussian quadrature rule and SGQ rule are also compared in Table 5, which clearly demonstrates again that the unified formula of complex ratio distribution shown in Eq. (31) can be computed using the SGQ rule more efficiently than the conventional multi-dimensional Gaussian quadrature rule when the analytical formula is not available.

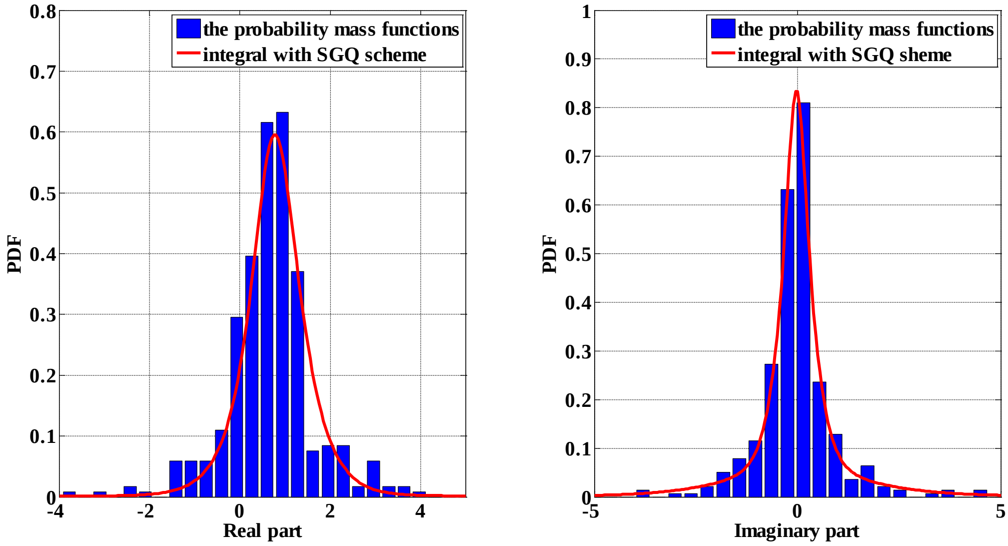

(a) Comparison of the probability mass function and the complex t ratio distribution computed using SGQ rule

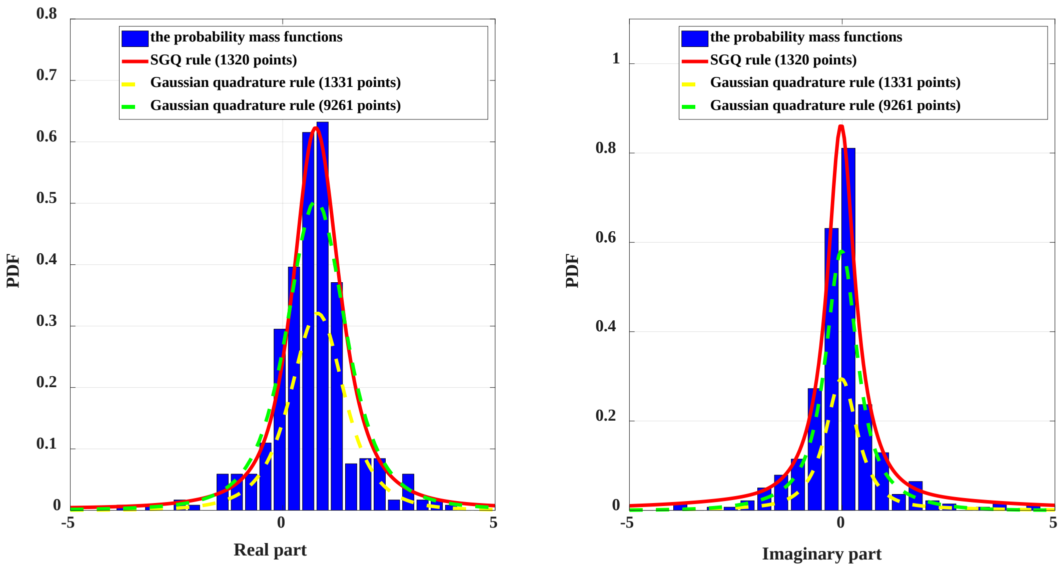

(b) Comparison of the numerical solution of complex t ratio distribution computed using SGQ rule (1320 quadrature points) and Quadratic rule (1331 and 9261 quadrature points)

Fig. 9: Marginal PDFs and the histogram of the real and imaginary parts of $T_{15}^{(\omega_k)}$ at $\omega_k = 4.31\pi$ rad/s

5.2 Performance evaluation using the test of Alamosa Canyon Bridge

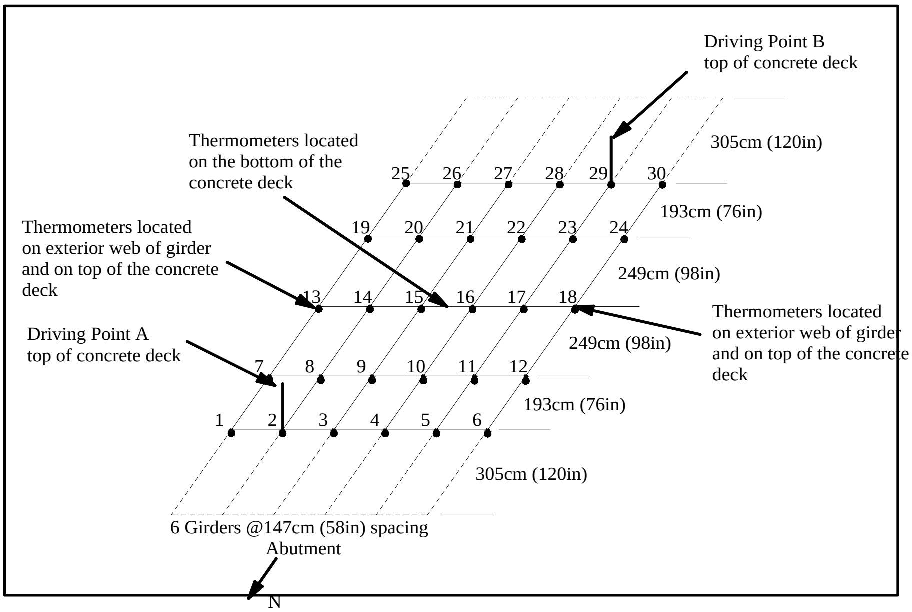

Fig. 10: Positions of the accelerometer of the Alamosa Canyon Bridge (from [64])

In this section, the performance of the unified solution of computing the complex ratio distribution is further evaluated by using the field test measurement of the Alamosa Canyon Bridge. This bridge is located approximately 16 km north of Truth or Consequences, New Mexico, USA [64]. The bridge has seven independent spans with each span consisting of a concrete deck supported by six steel beams. The roadway in each span is approximately 7.3 m wide and 15.2 m long. Expansion joints are located at both ends of each span. The concrete deck and the girders below the bridge were equipped with a total of 31 accelerometers as shown in Fig. 10.

This field test of the bridge was conducted on the bridge to study various issues related to bridge structural integrity. Owing to the efforts of the researchers from the Los Alamos National Laboratory, a website (http://ext.lanl.gov/projects/damage_id/) has been established for collecting various vibration test data as a benchmark problem. The field test data used in this study lasted 24 h, from July 21, 1997 to July 23, 1997. The sampling rate of the acceleration data is 128 Hz. The response measurements are segmented into 330 non-overlapping sequences with each one lasting 16 s. The FFT coefficients can be calculated accordingly for each sequence. As in MCS, each segment can be viewed as a random realization and one can be employed to draw the histograms to validate the accuracy of the theoretical PDF. By analyzing the measurements acquired from different sensors, the following analyses were conducted.

- For the FFT coefficients at a number of frequencies, the results of the K-S test suggest that the complex Gaussian probability model could not adequately capture the statistics of all samples, while the *t*-distribution can model FFT coefficients well at a number of frequencies well. The real and imaginary parts of $Y_{11}^{(\omega_k)}$ at $\omega_k = 11.5\pi$ rad/s and $\omega_k = 1.25\pi$ rad/s, respectively, are investigated in detail. Fig. 11(a) and 12(a) display the probability plots of the real part of $Y_1^{(\omega_k)}$ at $\omega_k = 11.5\pi$ rad/s and the imaginary part of $Y_1^{(\omega_k)}$ at $\omega_k = 1.25\pi$ rad/s, where the Gaussian and t distributions of the data are shown. The probability plots of the Gaussian and t distributions are denoted by the red straight line and blue line, respectively. As shown in Fig. 11(a), the scattered samples at $\omega_k = 11.5\pi$ rad/s lie on a curve that coincides with the straight red line, indicating that the Gaussian assumption was not violated for the given samples. However, the scattered samples of at $\omega_k = 1.25\pi$ rad/s shown in Fig. 12(a) were more consistent with the t location-scale distribution, even accounting for the tail. Fig. 11(b) and 12(b) show the histograms of the real part at $\omega_k = 11.5\pi$ rad/s and the imaginary part at $\omega_k = 1.25\pi$ rad/s, accompanied by the theoretical curves derived from the complex Gaussian and complex t models. This again indicates the superiority of the t location-scale distribution model for $Y_1^{(\omega_k)}$ at $\omega_k = 1.25\pi$ rad/s.

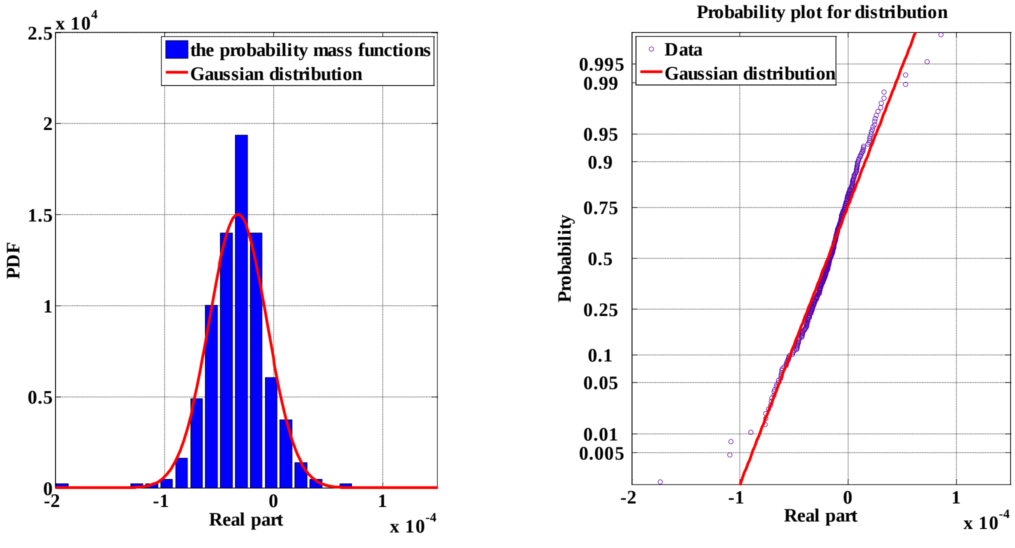

Fig. 11: Distribution properties of the real part of $Y_1^{(\omega_k)}$ at $\omega_k = 11.5\pi$ rad/s : (a) The theoretical marginal PDFs and the histogram; (b) the probability plot

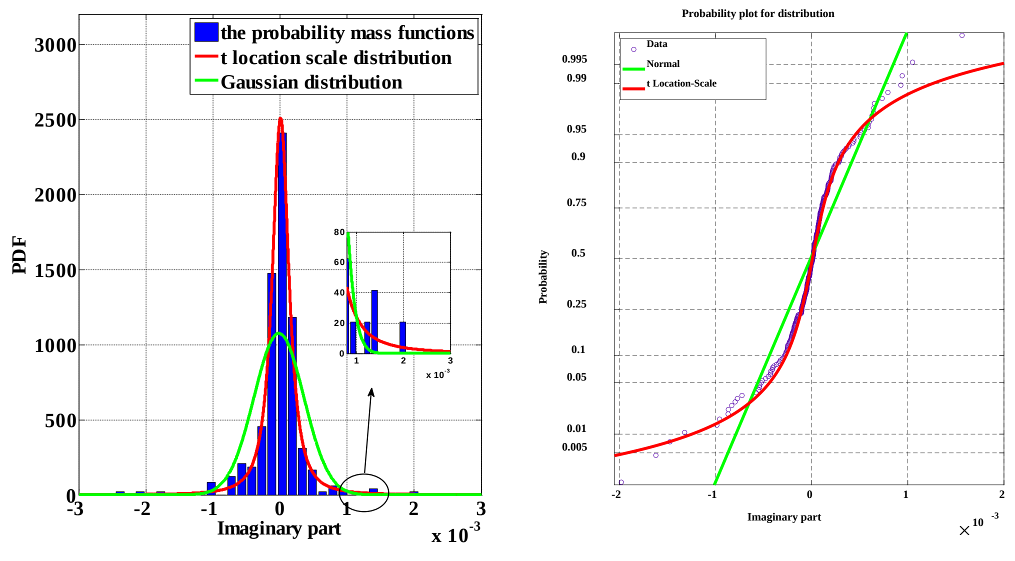

Fig. 12: Distribution properties of the imaginary part of $Y_1^{(\omega_k)}$ at $\omega_k = 1.25\pi$ rad/s : (a) The theoretical marginal PDFs and the histogram; (b) the probability plot

- $H_{3,1}^{(\omega_k)}$ at $\omega_k = 6.875\pi$ rad/s , which can be modelled using a complex-valued t ratio distribution, is observed. The variances of $F_3^{(\omega_k)}$ and $Y_1^{(\omega_k)}$ at $\omega_k = 6.875\pi$ rad/s are

4.925×10^{-5} and 5.410×10^{-5}, respectively, and their complex correlation coefficient is $0.1233+0.2384i$. Fig. 13 compares the complex-valued t ratio distribution of the real and imaginary parts of $H_{3,1}^{(\omega_k)}$ at $\omega_k = 6.875\pi$ rad/s denoted by solid lines, with the probability mass functions denoted by histograms drawn from all samples. Fig. 13 shows that the solid curves (i.e., Eq. (31)) obtained by the fast SGQ scheme agree well with the histograms, indicating the efficiency of the proposed method in inferring the statistics of the FRFs to following a complex non-Gaussian ratio distribution, the closed- form of which is difficult to achieve.

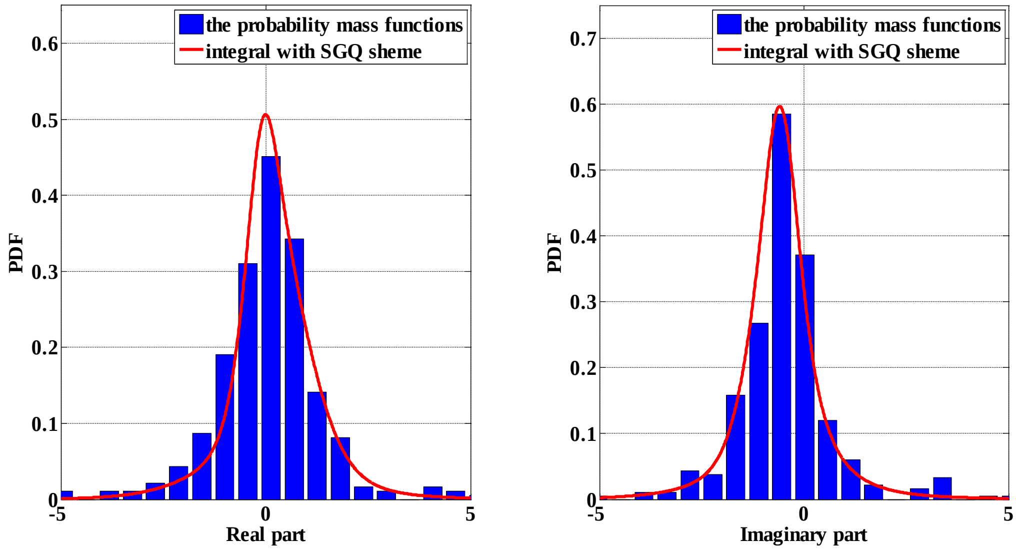

Fig. 13: Theoretical marginal PDFs and the histograms of the real and imaginary parts of $H_{3,1}^{(\omega_k)}$ at $\omega_k = 6.875\pi$ rad/s

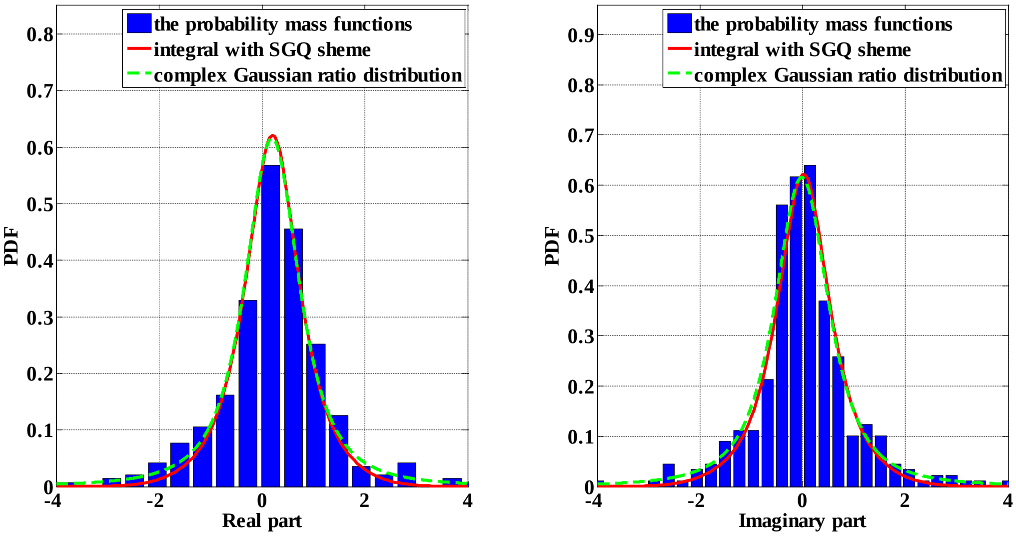

(a) $T_{11,1}^{(\omega_k)}$ at $\omega_k = 11.5\pi$ rad/s

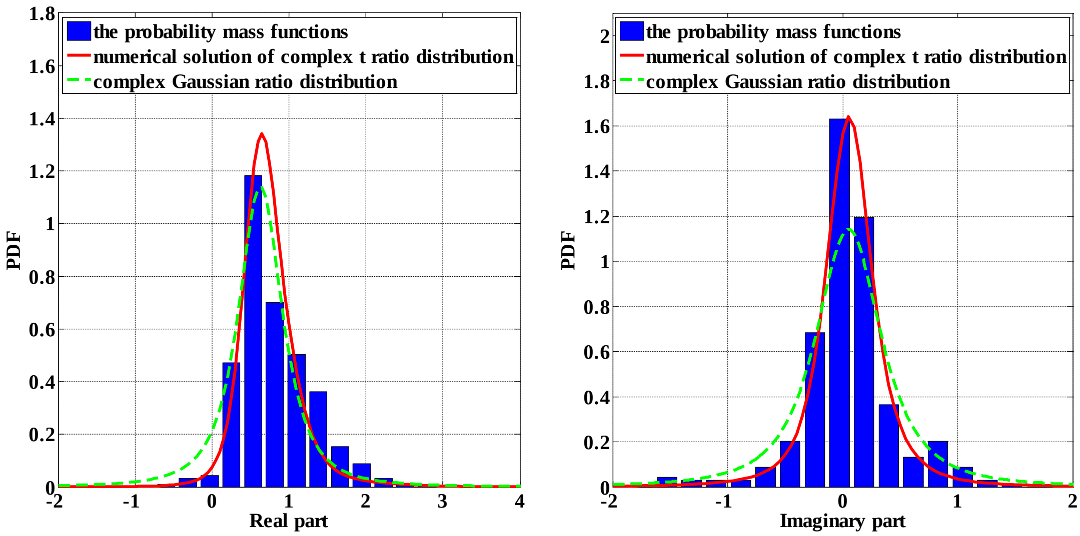

(b) $T_{11,1}^{(\omega_k)}$ at $\omega_k = 1.25\pi$ rad/s

Fig. 14: Theoretical marginal PDFs and the histogram PDFs of the real and imaginary parts of $T_{11,1}^{(\omega_k)}$ at $\omega_k = 11.5\pi$ rad/s and $\omega_k = 1.25\pi$ rad/s

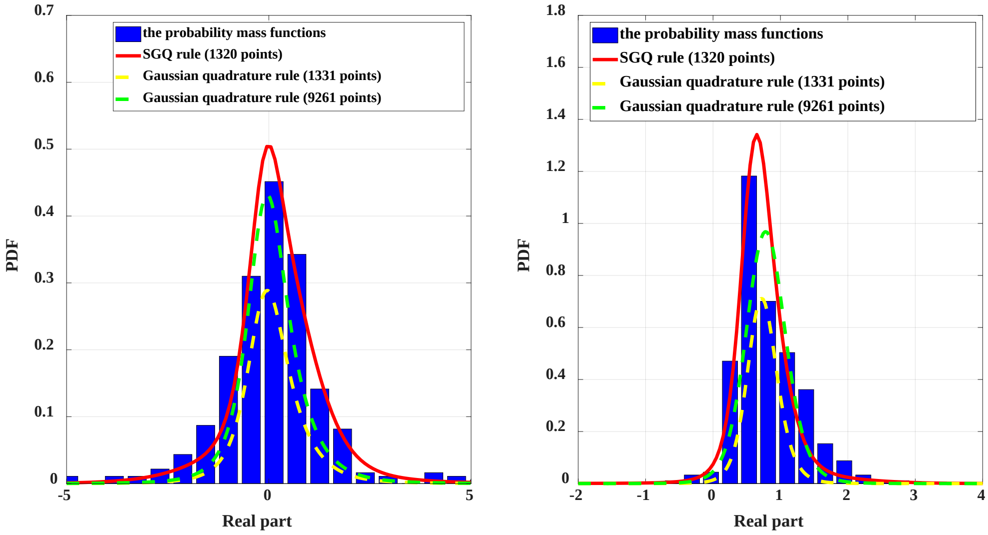

Fig. 15: Comparison of the theoretical marginal PDFs of $\left[H_{3,1}^{(\omega_k)}\right]^{\Re}$ at $\omega_k = 6.875\pi$ rad/s and $\left[T_{11,1}^{(\omega_k)}\right]^{\Re}$ at $\omega_k = 1.25\pi$ rad/s computed with SGQ rule (1320 quadrature points) and Quadratic rule (1331 and 9261 quadrature points)

- The TF $T_{11,1}^{(\omega_k)}$ corresponding to the 11th and first sensors at $\omega_k = 11.5\pi$ rad/s and $\omega_k = 1.25\pi$ rad/s are presented in Fig. (14). In Fig. 14(a), the solid line denotes the complex Gaussian ratio distribution computed with the SQG rule, while the dotted lines are plotted according to the closed-form formula of the complex Gaussian ratio distribution. In Fig. 14(b), the solid line denotes the complex t ratio distribution achieved by using the unified formula solved with the SQG rule, while the dotted lines denote the analytical formula of the complex Gaussian ratio distribution. Fig. 14(a) and (b) is accompanied by histograms denoting the probability mass functions of 330 samples. As is seen from Fig. 14(a), there is good consistency between the observed histograms, the curves of the analytical values, and the numerical values for both the real and imaginary parts. In Fig. 14(b), the t ratio distribution is a better candidate for modeling $T_{11,1}^{(\omega_k)}$ at $\omega_k = 1.25\pi$ rad/s. Furthermore, Fig.

14(a) and (b) verify that, given the accurate probabilistic model of FFT coefficients, the PDF of the TFs can be solved using the advanced numerical algorithm efficiently.

- To highlight the efficiency and accuracy of proposed algorithm, Fig.15 shows the complex t ratio probabilistic model of $\left[H_{3,1}^{(\omega_k)}\right]^{\Re}$ and $\left[T_{11,1}^{(\omega_k)}\right]^{\Re}$ at $\omega_k = 6.875\pi$ rad/s and $\omega_k = 1.25\pi$ rad/s computed using SGQ rule with 1320 quadrature points and Gaussian quadrature rule with 1331 and 9261 quadrature points. The time required for computing the PDF of $H_{3,1}^{(\omega_k)}$ and $T_{11,1}^{(\omega_k)}$, the marginal PDF of $\left[H_{3,1}^{(\omega_k)}\right]^{\Re}$ and $\left[T_{11,1}^{(\omega_k)}\right]^{\Re}$, as well as the expected values of $\left[H_{3,1}^{(\omega_k)}\right]^{\Re}$ and $\left[T_{11,1}^{(\omega_k)}\right]^{\Re}$ at $\omega_k = 6.875\pi$ rad/s and $\omega_k = 1.25\pi$ rad/s by the conventional Gaussian quadrature rule and SGQ rule are compared in Table 6. Compared with the Gaussian quadrature rule, the SGQ rule can achieve higher accuracy by involving significantly fewer quadrature points than Gaussian quadrature rule. Therefore, as is seen from Table 6, the time consumed by the SGQ rule is significantly less than that of the classic Gaussian quadrature rule. Therefore, the unified solution is expected to be efficient in quantifying the uncertainties of FRFs and TFs by integrating the unified formula of the complex ratio distribution with multi-dimensional integrals and the SGQ rule when it is difficult to find the closed-form solution.

Table 6: Time consumed by two different numerical strategies for the Alamosa Canyon Bridge

Items	PDFs	Gaussian quadrature		Sparse-grid quadrature	
		Time (s)	Quadrature points	Time (s)	Quadrature points
FRF at $\omega_k = 6.875\pi$ rad/s	PDF of $H_{15}^{(\omega_k)}$	73.61	441	8.02	377
	Marginal PDF of $\left[H_{15}^{(\omega_k)}\right]^{\Re}$	515.09	9261	18.93	1320

	Expectation of $\left[H_{15}^{(\omega_k)}\right]^{\Re}$	7277.20	194481	19.87	4433
TF at $\omega_k = 1.25\pi$ rad/s	PDF of $T_{15}^{(\omega_k)}$	67.28	441	7.33	377
	Marginal PDF of $\left[T_{15}^{(\omega_k)}\right]^{\Re}$	514.82	9261	18.91	1320
	Expectation of $\left[T_{15}^{(\omega_k)}\right]^{\Re}$	7064.78	194481	19.29	4433

6 Conclusions

A unified scheme to solving complex ratio distributions was developed and applied to statistical inference for FRFs and TFs. This development enlarges the capabilities of FRFs and TFs with the expectation to improve analyses in the areas of modal analysis and damage detection where FRFs and TFs are key tools. The classic complex Gaussian ratio distribution whose analytical PDF has been derived recently is being increasingly used to model the distributions of FRFs and TFs due to its elegant and convenient mathematical nature. However, the field-test data analysis of engineering structures, using FFT, confirmed the necessity to expand this concept to non-Gaussianity due to various reasons such as nonstationarity of the data, the limited length of the data available, etc. In order to work with the general case of FFT coefficients that follow complex non-Gaussian distributions, a unified scheme was proposed in this study that generalizes the initial closed-form approaches.

The theoretical findings of this study were verified using response measurements of a simply supported beam and the Alamosa Canyon bridge. Discrepancies between the analytical PDFs and corresponding histograms were plotted to display the accuracy of the probabilistic models. It is worth mentioning here that, the histogram of FRF and TF samples can be well predicted by the theoretical PDFs given that we can model the FFT samples well by a proper complex-valued probabilistic model. The time required for computing the PDF, the marginal PDF as well as the expectation of complex ratio distributions by Gaussian quadrature rule and

SGQ rule were also compared to highlight the great efficiency of the SGQ scheme. Results indicate that the unified computational probability model incorporating SGQ numerical algorithm proposed in this study can quantify the uncertainties of complex ratio random variables much more efficiently. This study yields new insights into the qualitative analysis of the uncertainty of FRFs and TFs, which paves the way for developing new statistical methodologies for dynamic inverse problems.

It is worth noting that the proposed algorithm is associated with the usual requirements for a stochastic analysis. Most importantly, the distribution of $\Theta=\{V \quad U\}^T$ should be known in advance to derive the complex-valued ratio distribution for U/V. Therefore, one should propose a proper probabilistic model for the denominator and the nominator before applying the proposed algorithm. In this present study, complex-valued Gaussian and t-distribution, which have been proved to be good candidates in [61] and [43], are used to characterize the distribution of FFT coefficients. Though this choice is probably quite representative, there are certainly cases when other distributions are more suitable. In any case, field-test data should be used to verify the suitability of the distributions for the FFT coefficients, for example via a K-S test. If distributions other than used in our approach are more suitable, the derivations shown need to be realized for those cases. This may involve some mathematical challenges and is certainly a valuable topic for further investigation. Our approach showing the principle of this derivation on a representative case forms the basis for such future expansion.

Acknowledgement

Financial support to complete this study was provided in part by Natural Science Foundation of China (No. 51778203 and 51778204), the Science and Technology Development Fund, Macau SAR (File no. SKL-IOTSC-2018-2020), the National Key Research and Development

Program of China (No. 2019YFB2102702) and Shenzhen Science and Technology Program (No. KQTD20180412181337494). Furthermore, the authors would thank Los Alamos National Laboratory for providing the data from the various vibration tests performed on the Alamosa Canyon Bridge to the public. The authors would like to thank Shi-Ze Cao and Long Yang, postgraduates at Hefei University of Technology, for their kind help in preparing for the specimen and conducting the experiment.

Reference

[1] F. Penna, R. Garello, M.A. Spirito, Cooperative spectrum sensing based on the limiting eigenvalue ratio distribution in Wishart matrices, IEEE Communications Letters, 13 (7) (2009) 507-509.

[2] J.B. Chen, and J. Li, Dynamic response and reliability analysis of non-linear stochastic structures, Probabilistic Engineering Mechanics, 20 (1) (2005) 33-44.

[3] J. Li, J.B. Chen, The probability density evolution method for dynamic response analysis of non−linear stochastic structures, International Journal for Numerical Methods in Engineering, 65 (6) (2006) 882-903.

[4] A. Sarrafi, Z. Mao, M. Shiao, Uncertainty quantification framework for wavelet transformation of noise-contaminated signals, Measurement, 137 (2019) 102-115.

[5] E. Díaz-Francés, F.J. Rubio, On the existence of a normal approximation to the distribution of the ratio of two independent normal random variables, Statistical Papers, 54 (2) (2013) 309-323.

[6] R.F. Kappenman, A Note on the Multivariate t-Ratio Distribution, The Annals of Mathematical Statistics, 42 (1) (1971) 349-351.

[7] D.L. Hawkins, C.P. Han, Bivariate distributions of some ratios of independent noncentral chi-square random variables, Communication in Statistics-Theory and Methods, 15 (1) (1986) 261-277.

[8] S. Nadarajah, A. K. Gupta, On the product and ratio of Bessel random variables, International Journal of Mathematics and Mathematical Sciences, 2005 (18) (2005) 2977-2989.

[9] D. Astély, B. Ottersten, The effects of local scattering on direction of arrival estimation with MUSIC, IEEE transactions on Signal Processing, 47(12) (1999) 3220-3234.

[10] R.J. Baxley, B.T. Walkenhorst, G. Acosta-Marum, Complex Gaussian ratio distribution with applications for error rate calculation in fading channels with imperfect CSI, Global Telecommunications Conference (GLOBECOM 2010), 2010 IEEE, Dec 2010, 1-5.

[11] M. M. Hyder, R. H. Khan, and K. Mahata, An enhanced random access mechanism for smart grid M2M communications in WiMAX networks, in Proc. IEEE International Conference on Smart Grid Communications (SmartGridComm), Nov. 2014, 356–361.

[12] S. Wu and B. L. Hughes, Training-based joint channel and antenna impedance estimation, in Proc. 52nd Annual Conference on Information Sciences and Systems, Mar. 2018, 1–6.

[13] S. Wu, B. L. Hughes, A hybrid approach to joint estimation of channel and antenna impedance, in Proc. 52nd Annual Conference on Information Sciences and Systems, Oct. 2018, 1-6.

[14] F.P. Itturriet, M.H. Costa, Perceptually relevant preservation of interaural time differences in binaural hearing aids. IEEE/ACM Transactions on Audio, Speech, and Language Processing, 27(4) (2019) 753-764.

[15] E.S. Nadimi, M.H. Ramezani, V. Blanes-Vidal, On the ratio of independent complex Gaussian random variables, Multidimensional Systems and Signal Processing, 29(4) (2018) 1553-1561.

[16] S. Nadarajah, H.S. Kwong, A note on “On the ratio of independent complex Gaussian random variables”, Multidimensional Systems and Signal Processing, 29(4) (2018) 1839-1843.

[17] Y. Li, Q. He, On the ratio of two correlated complex Gaussian random variables, IEEE Communications Letters, 23(12) (2019) 2172-2176.

[18] S. Wu, Moments of complex Gaussian ratios, IEEE Communications Letters, 23(1) (2018) 88-91.

[19] W.J. Yan, W.X. Ren, Circularly-symmetric complex normal ratio distribution for scalar transmissibility function. Part I: Fundamentals, Mechanical Systems and Signal Processing, 80 (2016) 58-77.

[20] W.J. Yan, W.X. Ren, Generalized proper complex Gaussian ratio distribution and its application to statistical inference for frequency response functions, Journal of Engineering Mechanics, 144 (9) (2018) 04018080.

[21] J. Antoni, Leakage-free identification of FRF's with the discrete time Fourier transform, Journal of sound and vibration, 294 (4) (2006) 981-1003.

[22] D. Moens, D. Vandepitte, An interval finite element approach for the calculation of envelope frequency response functions. International Journal for Numerical Methods in Engineering, 61(14) (2004) 2480-2507.

[23] Z. Mao, M.D. Todd, Statistical modeling of frequency response function estimation for uncertainty quantification, Mechanical Systems and Signal Processing, 38 (2) (2013) 333-345.

[24] Z. Mao, M.D. Todd, A model for quantifying uncertainty in the estimation of noise-contaminated measurements of transmissibility, Mechanical Systems and Signal Processing, 28 (2012) 470-481.

[25] W.J. Yan, W.X. Ren, Circularly-symmetric complex normal ratio distribution for scalar

transmissibility function. Part II: probabilistic model and validation, Mechanical Systems and Signal Processing, 80 (2016) 78-98.

[26] W.J. Yan, W.X. Ren, (2018). Circularly-symmetric complex normal ratio distribution for scalar transmissibility function. Part III: application to statistical modal analysis, Mechanical Systems and Signal Processing, 98 (2018) 1000-1019.

[27] N.M.M. Maia, J.M.M. Silva, E.A.M. Almas, R.P.C. Sampaio, Damage detection in structures: From mode shape to frequency response function methods, Mechanical Systems and Signal Processing, 17 (3) (2003) 489-498.

[28] N.M.M. Maia, R. Almeida, A.P.V. Urgueira, R.P.C. Sampaio, Damage detection and quantification using transmissibility, Mechanical Systems and Signal Processing, 25 (7) (2011) 2475-2483.

[29] K. Worden, Experimental validation of a structural health monitoring methodology: part I. Novelty detection on a laboratory structure, Journal of Sound and Vibration, 259 (2) (2003) 323-343.

[30] E. Papatheou, G. Manson, R.J. Barthorpe, K. Worden, The use of pseudo-faults for novelty detection in SHM, Journal of Sound and Vibration, 329 (12) (2010) 2349-2366.

[31] T.J. Johnson, D.E. Adams, Transmissibility as a differential indicator of structural damage, Journal of Vibration and Acoustics, 124 (4) (2002) 634-641.

[32] T.J. Johnson, R.L. Brown, D.E. Adams, M. Schiefer, Distributed structural health monitoring with a smart sensor array, Mechanical Systems and Signal Processing, 18 (3) (2004) 555-572.

[33] C. Devriendt, P. Guillaume, The use of transmissibility measurements in output-only modal analysis, Mechanical Systems and Signal Processing, 21 (7) (2007) 2689-2696.

[34] C. Devriendt, G.D. Sitter, P. Guillaume, An operational modal analysis approach based on parametrically identified multivariable transmissibilities, Mechanical Systems and Signal

Processing, 24 (5) (2010) 1250-1259.

[35] W.J. Yan, W.X. Ren, Operational modal parameter identification from power spectrum density transmissibility, Computer-Aided Civil and Infrastructure Engineering, 27 (3) (2012) 202-217.

[36] W.J. Yan, W.X. Ren, An Enhanced Power Spectral Density Transmissibility (EPSDT) approach for operational modal analysis: Theoretical and experimental investigation, Engineering Structures, 102 (2015) 108-119.

[37] R.M. Lin, J. Zhu, Model updating of damped structures using FRF data, Mechanical Systems and Signal Processing, 20 (8) (2006) 2200-2218.

[38] V. Meruane, Model updating using antiresonant frequencies identified from transmissibility functions, Journal of Sound and Vibration, 332 (4) (2013) 807-820.

[39] G.D. Sitter, C. Devriendt, P. Guillaume, E. Pruyt, Operational transfer path analysis, Mechanical Systems and Signal Processing, 24 (2) (2010) 416-431.

[40] Z.K. Peng, G. Meng, Z.Q Lang, W.M. Zhang, F.L. Chu, Study of the effects of cubic nonlinear damping on vibration isolations using harmonic balance method, International Journal of Non-Linear Mechanics, 47 (10) (2012) 1073-1080.

[41] W.J. Yan, M.Y. Zhao, Q. Sun, W.X. Ren, Transmissibility-based system identification for structural health Monitoring: Fundamentals, approaches, and applications. Mechanical Systems and Signal Processing, 117 (2019) 453-482.

[42] J.X. Mao, H. Wang, D.M. Feng, T.Y. Tao, W.Z. Zheng, Investigation of dynamic properties of long-span cable-stayed bridges based on one-year monitoring data under normal operating condition, Structural Control and Health Monitoring, 25(5) (2018) e2146.

[43] W.J. Yan, L. Yang, X. Yang, W.X. Ren, Statistical modeling for fast Fourier transform coefficients of operational vibration measurements with non-Gaussianity using complex-valued t distribution, Mechanical Systems and Signal Processing, 132 (2019) 293-314.

[44] S.A. Smolyak, Quadrature and interpolation formulas for tensor products of certain classes of functions, Doklady Akademii Nauk, 148 (1963) 1042-1045.

[45] G.W. Wasilkowski, H. Wozniakowski, Explicit cost bounds of algorithms for multivariate tensor product problems, Journal of Complexity, 11 (1) (1995) 1-56.

[46] F. Heiss, V. Winschel, Likelihood approximation by numerical integration on sparse grids, Journal of Econometrics, 144 (1) (2008) 62-80.

[47] R. Radhakrishnan, A.K. Singh, S. Bhaumik, N.K. Tomar, Multiple sparse-grid Gauss-Hermite filtering, Applied Mathematical Modelling, 40 (7-8) (2016) 4441-4450.

[48] J. He, S. Gao, J. Gong, A sparse grid stochastic collocation method for structural reliability analysis, Structural Safety, 51(2014) 29-34.

[49] J. Bin, X. Ming, C. Yang, Sparse-grid quadrature nonlinear filtering, Automatica, 48 (2) (2012) 327-341.

[50] S.C. Olhede, On probability density functions for complex variables, IEEE Trans. Inf. Theory, 2006, 52(3): 1212-1217

[51] G. Falsone, R. Laudani, Matching the principal deformation mode method with the probability transformation method for the analysis of uncertain systems, International Journal for Numerical Methods in Engineering, 118 (7) (2019) 395-410.

[52] B. Huang, X. Du, A robust design method using variable transformation and Gauss–Hermite integration, International Journal for Numerical Methods in Engineering, 66 (12) (2006) 1841-1858.

[53] D. Wang, K.L. Tsui, Q. Zhou, 2016. Novel Gauss-Hermite integration based Bayesian inference on optimal wavelet parameters for bearing fault diagnosis, Mechanical Systems and Signal Processing, 72 (2016) 80-91.

[54] V. Kaarnioja, Smolyak Quadrature, Master's thesis, University of Helsinki, 2013.

[55] G.H. Golub, J.H. Welsch, Calculation of Gauss quadrature rule, Mathematics of

Computation, 23 (106) (1969) 221-230
[56] S.K. Au, Operational Modal Analysis: Modeling, Bayesian Inference, Uncertainty Laws. Springer, 2017.
[57] W.J. Yan, L.S. Katafygiotis, A two-stage fast Bayesian spectral density approach for ambient modal analysis. Part I: Posterior most probable value and uncertainty, Mechanical Systems and Signal Processing, 54 (2015)139-155.
[58] W.J. Yan, L.S. Katafygiotis, An analytical investigation into the propagation properties of uncertainty in a two-stage fast Bayesian spectral density approach for ambient modal analysis. Mechanical systems and signal processing, 118 (2019) 503-533.
[59] J. Schoukens, R. Pintelo, Identification of Linear Systems: A Practical Guideline for Accurate Modelling, Automatica, 29 (6) (1993) 1621-1622
[60] R. Pintelon, Y. Rolain, W. Van Moer, Probability density function for frequency response function measurements using periodic signals, IEEE Transactions on Instrumentation and Measurement, 52 (1) (2003) 61-68.
[61] K.V. Yuen, L.S. Katafygiotis, J.L. Beck, Spectral density estimation of stochastic vector processes, Probabilistic Engineering Mechanics, 17 (3) (2002) 265-272.
[62] K.V. Yuen, Bayesian Methods for Structural Dynamics and Civil Engineering, John Wiley & Sons, 2010.
[63] L.S. Katafygiotis, K.V. Yuen, Bayesian spectral density approach for modal updating using ambient data, Earthquake engineering & structural dynamics, 30(8) (2001) 1103-1123.
[64] C. R. Farrar, P. J. Cornwell, S. W. Doebling, M. B. Prime, Sturctural health monitoring studies of the Alamosa canyon and I-40 Bridges. Los Alamos National Laboratory report, LA-13635-MS, 2000.